Urbanization exacerbates continental- to regional-scale warming

Graphical abstract

Highlights

- Massive increases seen in urban area throughout countries and continents

- Urban warming signal has become strong enough to detect at larger scales

- However, primary cause of global warming is still not urbanization

- Given expected future urbanization, important to resolve these impacts
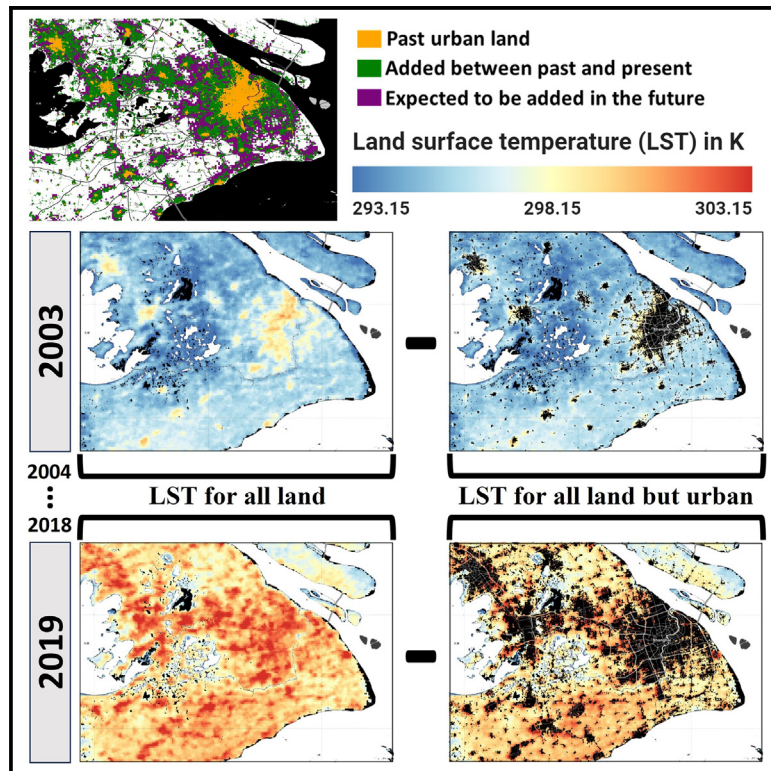
Authors

TC Chakraborty, Yun Qian

Correspondence

tc.chakraborty@pnnl.gov

In brief

Urban impacts on climate are generally discussed at the local scale, with urban areas ignored in large-scale climate assessments. We show that urbanization can intensify large-scale warming, especially in rapidly urbanizing regions and countries in Asia. Future urban growth will also influence continental-to regional-scale warming signals. These results fundamentally reframe how both the research community and the public usually think about urbanization, from only a local-scale phenomenon to one with non-negligible regional- and even continental-scale impacts.

CellPress

One Earth

CellPress
OPEN ACCESS

Article

Urbanization exacerbates continental-to regional-scale warming

TC Chakraborty[1,2,*] and Yun Qian[1]
[1]Pacific Northwest National Laboratory, Richland, WA, USA
[2]Lead contact
*Correspondence: tc.chakraborty@pnnl.gov
https://doi.org/10.1016/j.oneear.2024.05.005

SCIENCE FOR SOCIETY   Combining millions of satellite-derived images of land surface temperature (LST) with dynamic urban area estimates, we demonstrate that the urban influence on continental- to regional-scale warming has become more detectable over time, especially for rapidly urbanizing regions and countries in Asia. However, the main cause of global warming is still not urbanization, contributing to only around 2% of the land warming during the study period. We also estimate these large-scale urban warming signals under all shared socioeconomic pathways (SSPs) used to project global and regional climate change. Based on these results, we argue that, in line with other forms of land use/land cover change, urbanization should be explicitly included in future climate change assessments across scales. These patterns, also seen for air temperature, reframe our understanding of urbanization in the climate system from only a local-scale phenomenon to one with non-negligible regional- and even continental-scale impacts.

SUMMARY

Urbanization is usually ignored when estimating past changes in large-scale climate and for future climate projections since cities historically covered a small fraction of the Earth's surface. Here, by combining global land surface temperature observations with historical estimates of urban area, we demonstrate that the urban contribution to continental- to regional-scale warming has become non-negligible, especially for rapidly urbanizing regions and countries in Asia. Consequently, expected urban expansion over the next century suggests further increased urban influence on large-scale surface climate in the future (approximately 0.16 K for North America and Europe for high-emission scenario in 2100). Based on these results, also seen for air temperature, we argue that, in line with other forms of land use/land cover change, urbanization should be explicitly included in climate change assessments. This requires incorporation of dynamic urban extent and biophysics in current-generation Earth system models to quantify potential urban feedback on the climate system across scales.

INTRODUCTION

Changes in land use/land cover (LULC) modulate the Earth's climate through both biophysical and biogeochemical pathways.[1,2] These impacts, although highly uncertain, are large enough to be explicitly considered in future climate projections.[3] This was done initially for the Coupled Model Intercomparison Project Phase 5 (CMIP5) and is being expanded upon in Coupled Model Intercomparison Project Phase 6 (CMIP6) with the incorporation of more accurate transient LULC data.[3] However, urbanization, one of the most visible anthropogenic modifications of the terrestrial surface, is usually not accounted for when examining global climate.[4] The effect of urban areas on climate at these large scales is omitted or coarsely represented because

they traditionally covered a tiny fraction of the Earth's surface. For observational estimates of historical climate change, this involves setting up and selecting weather stations located away from cities and adjusting for possible urban contamination of the climatological record.[5–7] For models, this omission is built-in due to the lack of detailed urban representation in most Earth system models (ESMs).[4,8]

At the local scale, however, the physical process of urbanization—the replacement of natural land cover with built-up structures—can significantly modify surface climate through biophysical pathways.[9] These pathways include changes in surface reflectivity or albedo (α), reduction in evapotranspiration, changes in momentum and other energy fluxes, etc.[9,10] Many studies have examined these local-scale impacts of

urbanization, particularly on surface and near-surface temperature, commonly described by the urban heat island (UHI) effect.[9–15] Previous observational studies have also attempted to calculate whether urbanization has any measurable impact on large-scale climatology and climatological trends with mixed results.[5,6,16–21] Recently, several studies over mainland China have shown detectable impact of urbanization on regional and even national climate,[19,22,23] although similar studies are rare over other regions and countries.

The bulk of the research on possible urban influence (rather, bias due to urbanization) on large-scale temperature trends has been undertaken using or complemented by weather station measurements of 2 m air temperature (AT). Since weather stations are generally placed away from the urban core to avoid possible contamination,[5,24–26] these *in situ* AT measurements are not appropriate for estimating the impact of urbanization and its spatial heterogeneity on large-scale climate. Furthermore, there are major sampling biases in AT measurements, with dearth of observations in many rapidly urbanizing countries and other inhomogeneities over long periods.[5,7,24,26] Of note, the urban-rural classification of stations is difficult if regions are rapidly developing over the study period. While regional climate models can be used to detect the impact of urban development and expansion on the broader climate,[27,28] these urban models have large uncertainties and are expensive to run at the global scale.[29]

The availability of more than two decades of spatially complete satellite observations of emitted infrared radiation provides an opportunity to address some of these homogeneity issues and detect the urban signal on terrestrial climate using a different but complementary measure of temperature—the LST. Urban climate studies in the remote sensing literature have often used LSTs, but with a focus on the UHI effect, also called the surface UHI when quantified using LSTs.[11,13–15] Thus, most of the LST-based studies on urban climate, whether over single or multiple cities,[30] focus on this local impact of urbanization on warming, usually as the difference in LST of the urban area and its neighboring rural reference area.[31]

Here, we use these same satellite observations to ask a different but fundamental question about the role of urbanization on our planet—do cities and their changes, including lateral growth, have a detectable influence on large-scale climate? We demonstrate that urban influence on continental- to regional-scale LSTs (and also for AT based on a global AT dataset that accounts for urban areas) is non-negligible in recent decades, partly due to rapid urban expansion, as seen for multiple estimates of historical urban land cover, particularly over Asia. Moreover, expected future urbanization for different SSPs suggest further increases in this urban contribution to larger scale surface climate signals.

RESULTS

Historical urban expansion

Between 1992 and 2019, global urban area increased by approximately 226% (from 0.256% to 0.577%) based on the European Space Agency's Climate Change Initiative (ESA CCI) land cover data (0.13% of the global terrestrial surface per decade) (Figures 1 and S1). Put another way, 448,113.6 km^2 of urban land

was added globally between 1992 and 2019 (178,630.6 km^2 per decade). At the continental scale, the highest percentage increases were in Asia (312%) and Africa (251%), with the lowest changes in Oceania and other islands (approximately 155%). At country scale, there are large variations, with the Netherlands in Europe and Aruba in the Caribbean showing a more than 1,500% increase and nations like Iceland and Greenland showing practically no change (Figure 1A). For countries with populations exceeding 200 million (China, India, United States, Indonesia, Brazil, and Pakistan), the percentage changes in urban area are 413%, 366%, 181%, 179%, 205%, and 864%, respectively (108,446.3, 21,284.1, 64,831.5, 7,341.8, 13,663.3, and 4,228 km^2, respectively, of new urban land added between 1992 and 2019). Among the 20 countries with the most urban area, China and the United States show the largest decadal urban area growth (43,517.8 and 25,088.4 km^2 per decade, respectively), while Japan, Germany, and Ukraine show the strongest decadal urban growth as a percentage of the national land area (1.36%, 1.4%, and 1.14% per decade, respectively) (Figures 1C and 1E). Similarly, major urban expansion is also seen between 2003 and 2019 (Figures S1, and S2), the main time period of the LST analysis below. Note that we use the 2003 and 2019 period for this analysis since the most robust LST estimates are available for this period from the moderate resolution imaging spectroradiometer (MODIS) sensor onboard the Aqua satellite.[32] We also use a different satellite-derived LST estimate (from Landsat[33]; see discussion and experimental procedures) with greater uncertainty to confirm the consistency of these urban warming signals for the entire 1992 to 2019 period, as well as its subperiods.

Urban signal on temperature trends across scales

To isolate the urban temperature or warming signal, we first calculate continental-to regional-scale annual LST values for two scenarios, one including the yearly urban pixels and one without. The trends (regressed against the year) of the difference between these two scenarios (ΔLST_u) give the urban contributions to the overall trends. An illustrative schematic of this approach for the highly urbanized Shanghai metropolitan region is shown in Figure 2 and the time series for overall LST and the urban LST signal for all continents and the world are in Figure S3. Between 2003 and 2019, there was a decadal, statistically significant increase in daytime (0.4 ± 0.12 K per decade at approximately 1:30 p.m. local time) (Figure 3A) and nighttime (0.48 ± 0.11 K per decade at approximately 1:30 a.m. local time) (Figure 3D) LST from Aqua satellite observations for global land. The continental-scale LST trends during daytime were generally not significant (p ≥ 0.05), except for Asia and Europe. For nighttime, only North America showed non-significant increasing trends (Figure 3D). Europe shows the strongest daytime LST trends, which may partly be due to strong solar brightening during this period.[34] These trends are almost identical when we examine the Terra satellite observations from 2001 to 2019 (Figure S4).

Unlike the relatively (statistically) weak continental-scale trends in overall daytime LST, the urban LST signal is statistically significant for almost all cases, with the strongest trends seen for North America during daytime (0.01 K per decade) (Figure 3B) and for Asia at night (0.013 K per decade) (Figure 3E). The global
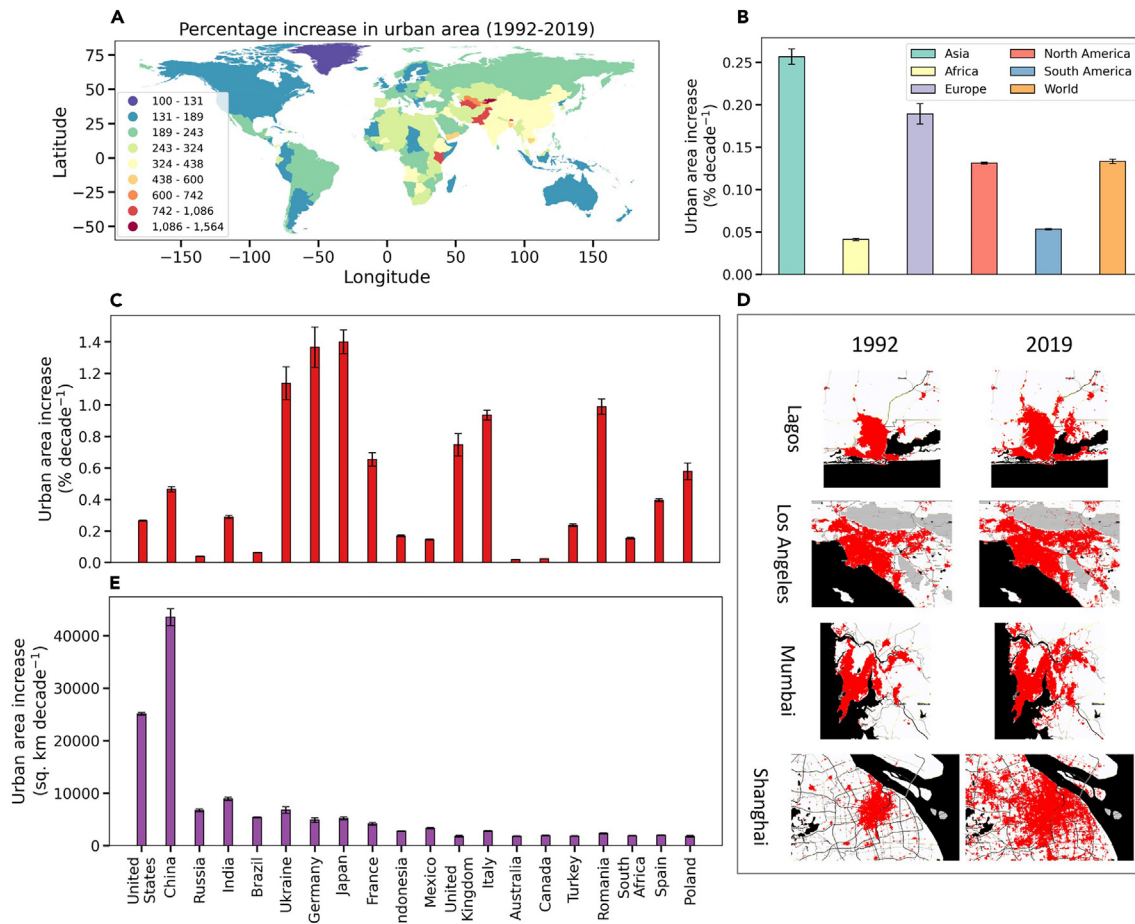
Figure 1. Long-term changes in urban area at multiple scales

(A) shows a global map of country-wise percentage increase in urban area between 1992 and 2019.

(B and C) show decadal rate of change in percent of urban area at continental scale and for the 20 most urbanized countries (in 2019), respectively.

(D) illustrates urban extent (red pixels) in 1992 and 2019 for a few select cities. Water pixels are in black.

(E) Similar to (C), but for growth in urban area per decade. The error bars in (B), (C), and (E) give standard errors of the slopes of the linear least-squares regressions. All changes are statistically significant (p < 0.0001).

urban LST signal is 0.005 K per decade during daytime and 0.006 K per decade at night. Dividing the urban signal by the overall trends gives the fractional urban contribution to the trend. The global fractional urban contributions are small though non-negligible for both day (0.013 or 1.3%) and night (0.011 or 1.1%). Across continents, the urban contribution is largest for North America during daytime (0.037 or 3.7%). Moreover, barring Russia, Asia shows large urban contributions at around 0.08 during daytime and 0.05 at night.

Among the 20 largest countries, China and Japan tend to show large urban fractional contributions (can exceed approximately 0.25 during daytime for both), although this depends strongly on the time of day (Figures S5 and S6). We also calculate the urban warming signals for the Yangtze River Basin (YRB), Yangtze River Delta (YRD), and Indo-Gangetic Basin (IGB), three heavily populated and rapidly urbanizing regions in Asia, which is the fastest urbanizing continent (Figure 1B). The YRB region covers most of southeastern China and is home to more than 480 million people or one-third of China's population (Figure 4A). Between

1992 and 2019, the urban percentage in YRB rose from 0.33% to 1.57%. The YRD region, which is adjacent to the YRB and encompasses Shanghai and several other rapidly growing cities, has a population of around 175 million, with the urban percentage increasing from 1.44% in 1992 to 8.35% in 2019, making it one of the most urbanized regions in the country.[35] Finally, the IGB region, which covers part of Pakistan, most of North India, and Bangladesh, has a population exceeding 750 million, with the urban percentage increasing from 0.28% in 1992 to 1.4% in 2019. Two of these regions, the YRB and YRD, show large fractional urban contributions to LST, particularly during the daytime. For YRB, the daytime fractional contribution crosses 0.39 and it is approximately 0.19 and approximately −0.02 for the YRD and IGB, respectively. Interestingly, the daytime urban LST signal in the YRD is much higher at approximately 0.12 K per decade (versus 0.04 K per decade for the YRB), but the urban fractional contribution is lower than that in the YRB (approximately 0.19) because of the larger overall rate of change in daytime LST in the delta (Figure 4B). Note that the daytime urban
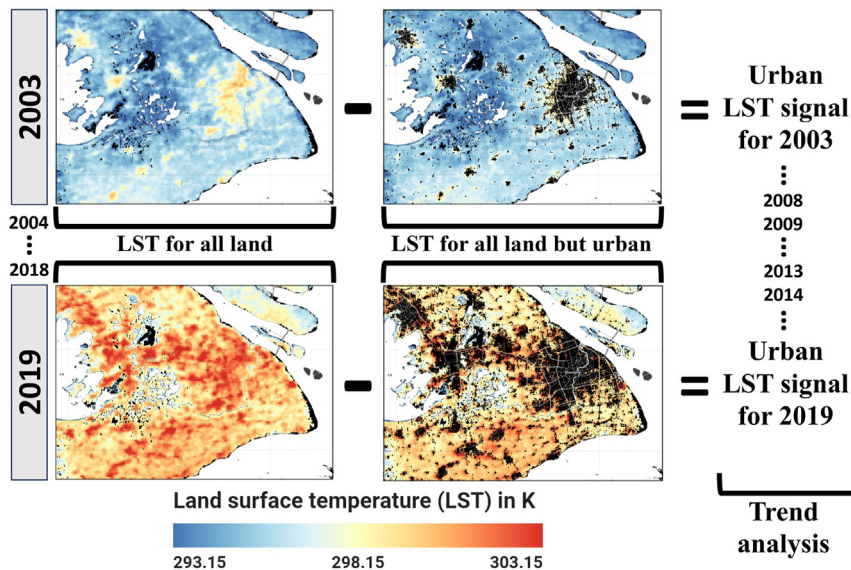
Figure 2. Schematic of methodological approach

An overview of the approach used to estimate urban warming signals from regional to continental scales in the present study illustrated over the Shanghai metropolitan region in China. The urban LST signal for each year is given by the difference in regionally averaged LST for all land pixels and all but urban land pixels. Trend analysis based on all the annual signals provide bulk estimates of urban contribution to large-scale warming. See experimental procedures for more details.

LST signal is negative for the IGB and positive for YRB. This is in line with the sign of the daytime surface UHI in these regions (positive over most cities in the YRB, and slightly negative over parts of the IGB[11,36]) and relates to land cover transitions during the urbanization process (also see example for Africa below).

Urban temperature signals and increased urbanization

The urban LST signals can be expressed as strong functions of urban percentage at various scales (Figures 4E–4G and 5). The sensitivities of the linear relationships are generally positive, i.e., the urban LST signal increases as more land becomes urbanized, which makes conceptual sense. However, there are exceptions to this rule. For instance, among the continents, Africa shows a negative sensitivity (-0.016 ± 0.001 K per urban %) during daytime (Figure 5A), which mirrors the small (sometimes negative) surface UHI magnitudes in drier climate.[10–12] This is due to differences in land cover transitions associated with urbanization in dry climate (versus wet climate), with urban areas cooling more efficiently than arid landscapes.[10] The strongest sensitivities are for North America for both day (0.087 K per urban %) and night (0.062 K per urban %). Since these sensitivities are indirect functions of the time period considered and the land cover dataset, we test various combinations of these two factors and find generally consistent results (Figures 5C and 5D; see experimental procedures). We should note here that the urban LST signal is the overall result of not just urban expansion (although we plot the LST signal against urban percentage), but also changes in other urban surface and atmospheric properties within the historical urban extents (for instance, densification, greening, and air pollution), which we collectively refer to as "urbanization" for simplicity. However, to avoid confusion with population-based definitions of urbanization,[37] in the future, we should use more clarifying terminology (say, "urban evolution") to refer to this combination of changes in urban extent and properties.

Although LST observations are limited to the satellite age, these strong sensitivities can give us potential contributions to the temperature signal over global land for pre-industrial period and future projections. For North America for instance, this contribution was practically zero in 1880 (0.008% urban) and can rise to 0.17 K (during daytime; 0.12 K at night) in 2100 for SSP5 (1.9% urban) (Figure 6). Globally, the contribution can rise to around 0.05 K for SSP5 (for both daytime and nighttime). This estimate may be on the lower end, since higher urban percentages are predicted for future scenarios in another dataset (Figure S7), with the global urban LST contribution rising to 0.12 K for daytime (0.11 K for nighttime). With the mean global warming expected to be around 4.2 K (50% probability; note that this is for AT) compared with pre-industrial levels by 2100 corresponding with SSP5,[38] the urban contribution to warming during daytime over land as a percentage of global warming may be between approximately 1.2% (Figure 6) to approximately 2.9% (Figure S7), which is small yet non-negligible and ignores potential feedback (both positive and negative) due to the purely data-driven method used in the present study. This percentage is generally similar across scenarios (e.g., 1.4%–2.5% for SSP2), but would also be a strong function of the emission pathway associated with the SSP scenario.

DISCUSSION

To minimize bias due to urbanization, *in situ* AT observations are frequently made away from urban cores, with many weather stations located at nearby airports.[14,26] As such, these measurements cannot capture the heterogeneity of the urban environment,[5,24] and thus its contribution to large-scale climate. In contrast, in some regions, such as in China,[7] urban (or urban adjacent) AT measurements may be more common than measurements in rural areas, leading to a different sampling bias. When using *in situ* measurements, determining the extent of urbanization's contribution to observed climate trends depends on how an urban weather station is defined.[21,26] Here, we take advantage of global spatially continuous observations of LST from the same sensor to isolate this signal in combination with dynamic land cover data. By essentially being a population-level sampling of almost all pixels over land, this method eliminates the biases due to the irregular placement of weather stations and the varied definitions of urban weather stations. Although LST and AT are physically distinct variables, particularly relevant for urban surfaces,[13] they are generally coupled at annual scales
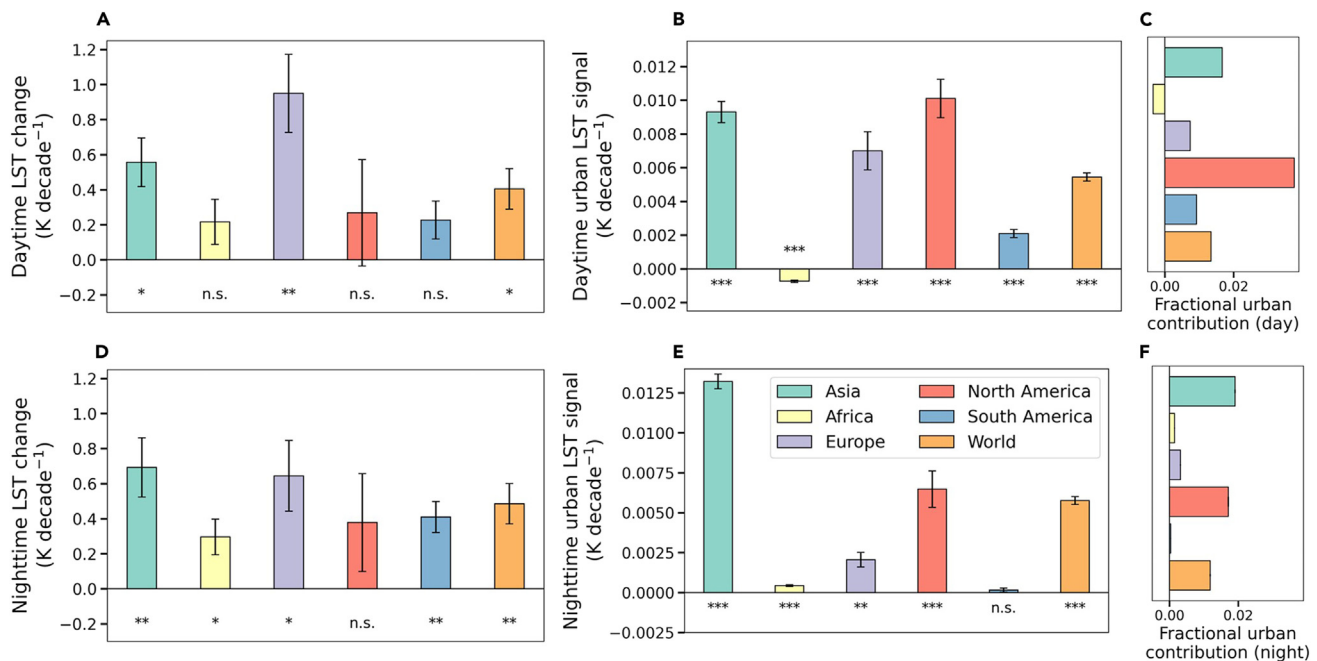
CellPress

OPEN ACCESS

Figure 3. Continental-scale trends in LST and urban contributions to them

(A) Decadal rates of change in continental-scale and global daytime (approximately 1:30 p.m. local time) LST with urban pixels included based on satellite observations from 2003 to 2019.

(B) Isolates the contribution from only urban pixels (trends in the LST difference between scenario including the urban pixels and scenario without).

(D and E) Similar to (A) and (B), but for nighttime (approximately 1:30 a.m. local time).

(C and F) Trends in the urban signal as a fraction of overall continental-scale trends in LST. The error bars give standard errors of the slopes of the linear least-squares regressions and the number of * below each bar gives level of statistical significance of the correlations (***p < 0.0001; **p < 0.001; *p < 0.01; n.s., p ≥ 0.05).

and for large regions. For instance, land AT has increased 0.30 K per decade between 2003 and 2019[39] compared with the 0.40 K per decade (for daytime; 0.48 K at night) seen here for LST (Figure 3A). This is also seen from the similar sensitivities to urban percentage in maximum and minimum AT (compared with daytime and nighttime LST) computed using a recent gridded dataset that accounts for urban areas (0.35 K and 0.43 K increases per urban percentage for maximum AT and daytime LST, respectively, for global land) (Figures 5A and S8A). However, LST provides stronger lower boundary constraints to the atmospheric column than AT by modulating the surface energy budget and boundary layer meteorology, making it important for climate-related feedback,[40] which was the primary goal behind isolating these urban signals in the present study.

Our satellite-derived estimates capture well established AT trends, including the stronger nighttime warming for global land surfaces.[41,42] Exact comparisons with estimates of decadal trends in the urban warming signals from most previous studies are difficult due to the AT sampling bias, different time periods used, and different objectives (examining bias due to urbanization rather than actual urban impact on larger scale AT). However, our trends in urban LST signals are similar to published values for AT over China (0.03 and 0.05 K per decade during day and night, respectively, vs. 0.05 K per decade in Zhou et al.[18]) and the United States (0.022 and 0.015 K per decade during day and night, respectively, vs. 0.027 K per decade in Kalnay and Cai[16]) using the observation minus reanalysis method. Many of

these weather station-based estimates of urban bias to climatological trends focused on the twentieth century. From 1992 to 2019, global urban area grew from 0.26% to 0.6%, which is more than the growth for the 100 years before that. As such, even if urban contribution to the climate signal was negligible back in the 2000s, this is becoming less true as the world urbanizes.

The urban LST signals calculated from isolating urban pixels may be conservative, since urbanization can influence neighboring non-urban pixels.[36] Similarly, the urban AT signals (Figure S8) may be conservative since advection can carry the urban influence downwind of the urban core.[43] The clear urban signal on continental-scale LST is also confirmed when we use two other annually varying land cover datasets and from Landsat-based LST estimates from 1992 (Figures 5C and 5D). Therefore, we are confident in the role of urbanization on continental-scale LSTs from these results. Of note, our estimates are several times higher than a recent study on the urban impact on global LSTs using a space-for-time approach.[44] For instance, for the SSP5 scenario at the end of the century, the urban daytime contribution to LSTs over Europe is around 0.16 K in the present study (Figure 6) (over 0.30 K from Figure S7) versus only 0.04 K in Zhou et al.[44] However, Zhou et al.[44] extrapolated from only three years (2014–2016) of MODIS Aqua observations instead of using the full time series of observations—with multiple estimates of historical land cover change and future projections of urbanization—as done here. As more years of various observations,
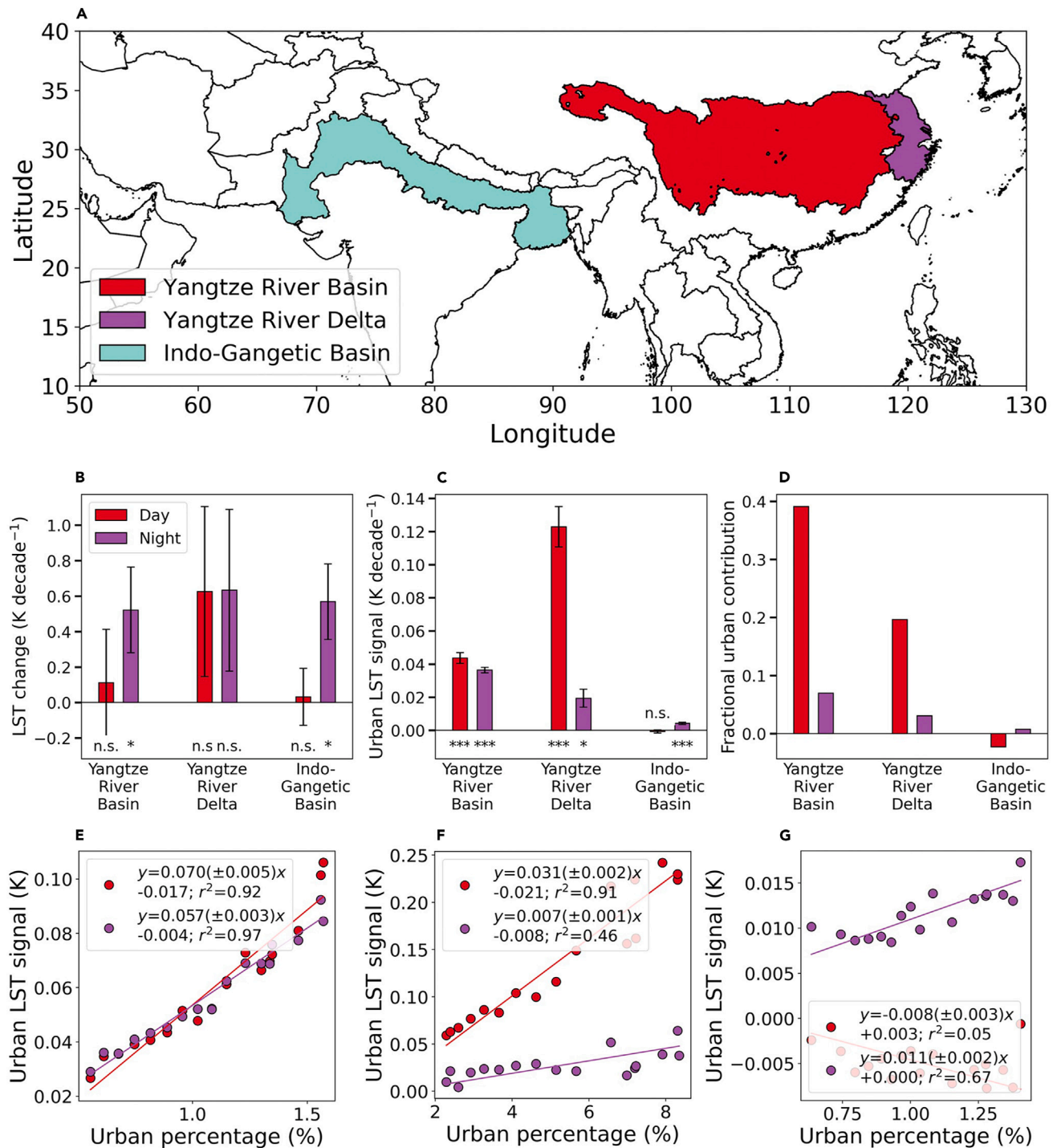
Figure 4. Urban temperature signal for three regions of interest

(A) The extent of the regions of interest—the YRB, the YRD, and the IGB.

(B) Decadal rates of change in regional daytime (approximately 1:30 p.m. local time) and nighttime (approximately 1:30 a.m. local time) LST with urban pixels included based on satellite observations from 2003 to 2019.

(C) Isolates the contribution from only the urban pixels.

(D) Trends in the urban signal as a fraction of the overall regional-scale trends. The error bars in (B) and (C) give the standard errors of the slopes of the linear least-squares regressions and the number of * below each bar gives the level of statistical significance of the correlations (***$p < 0.0001$; **$p < 0.001$; *$p < 0.01$; n.s. for $p \geq 0.05$).

(E–G) Associations between the yearly (2003–2019) urban signal on daytime and nighttime LST and the corresponding urban percentage for the YRB, YRD, and IGB, respectively. The lines of best fit, including the standard errors of the slopes, and the coefficients of determination are noted for these cases.
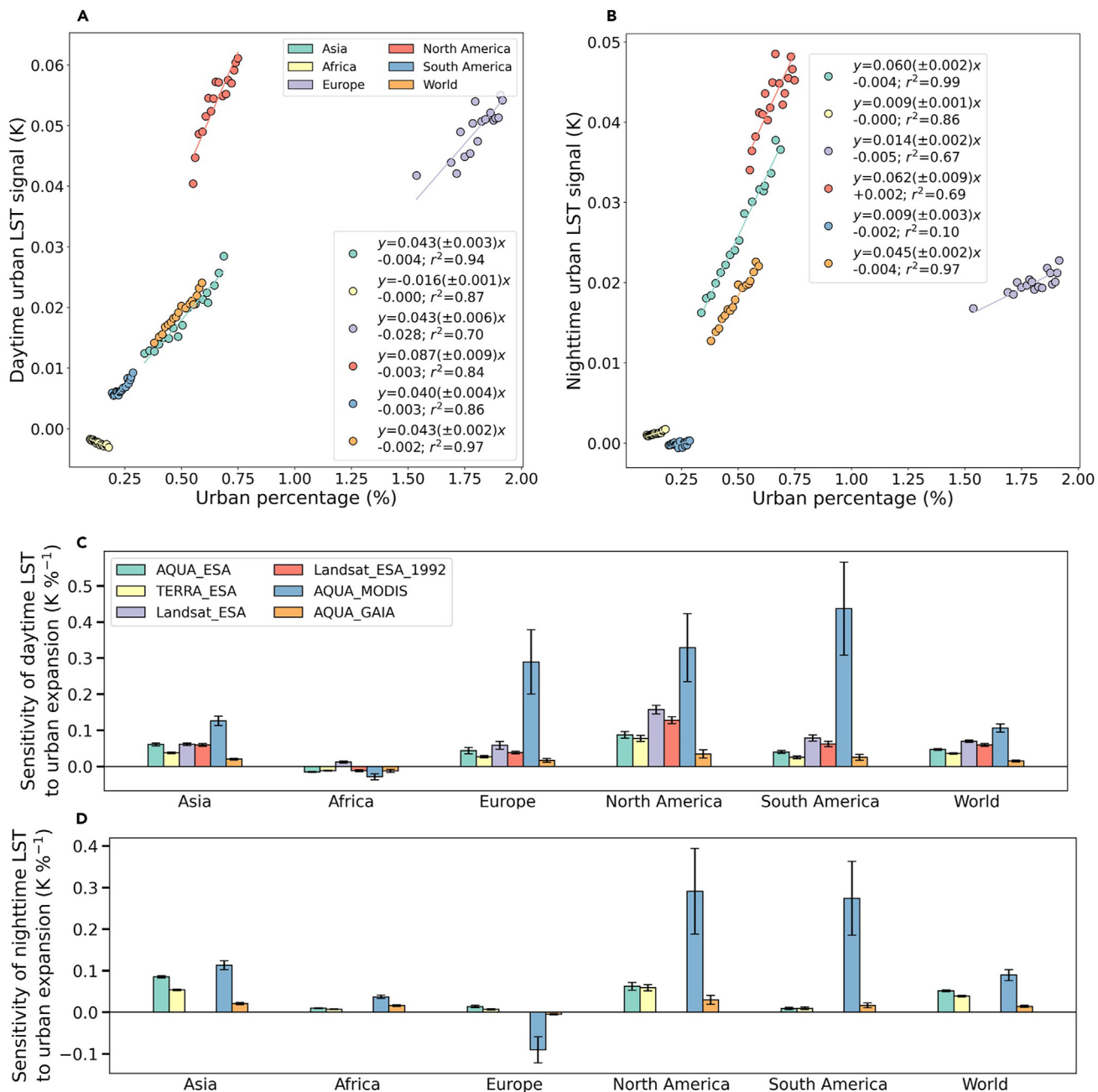
Figure 5. Associations between the urban temperature signal and urban percentage

(A) Associations between the yearly (2003–2019) urban signal on daytime (approximately 1:30 p.m. local time) LST and corresponding urban percentage for continental and global scales.

(B) Similar to (A), but for nighttime (approximately 1:30 a.m. local time). The lines of best fit, including standard errors of the slopes, and coefficients of determination are noted for all cases.

(C and D) Sensitivities (slopes; standard errors of slopes given by the error bars) from different data sources and time periods, including the MODIS Aqua (AQUA_ESA) and Terra (TERRA_ESA) estimates, Aqua estimates using the MODIS and global artificial impervious area (GAIA) land cover datasets (AQUA_MODIS and AQUA_GAIA, respectively), and from Landsat for two different periods (2003–2019 for Landsat_ESA and 1992–2019 for Landsat_ESA_1992).

including satellite data, are collected, future studies can further test the robustness of these trends using longer time periods and multiple data sources.

ESMs, our best tools for understanding the natural world at the process level, are currently ill-equipped to isolate urban contri-

butions to climate change, with the few global models incorporating urban land cover doing so in simplistic manners.[45–47] For instance, the Community Land Model, used in several large-scale urban studies,[10,48,49] has fixed urban extent and thus cannot isolate the important impacts of urban change and
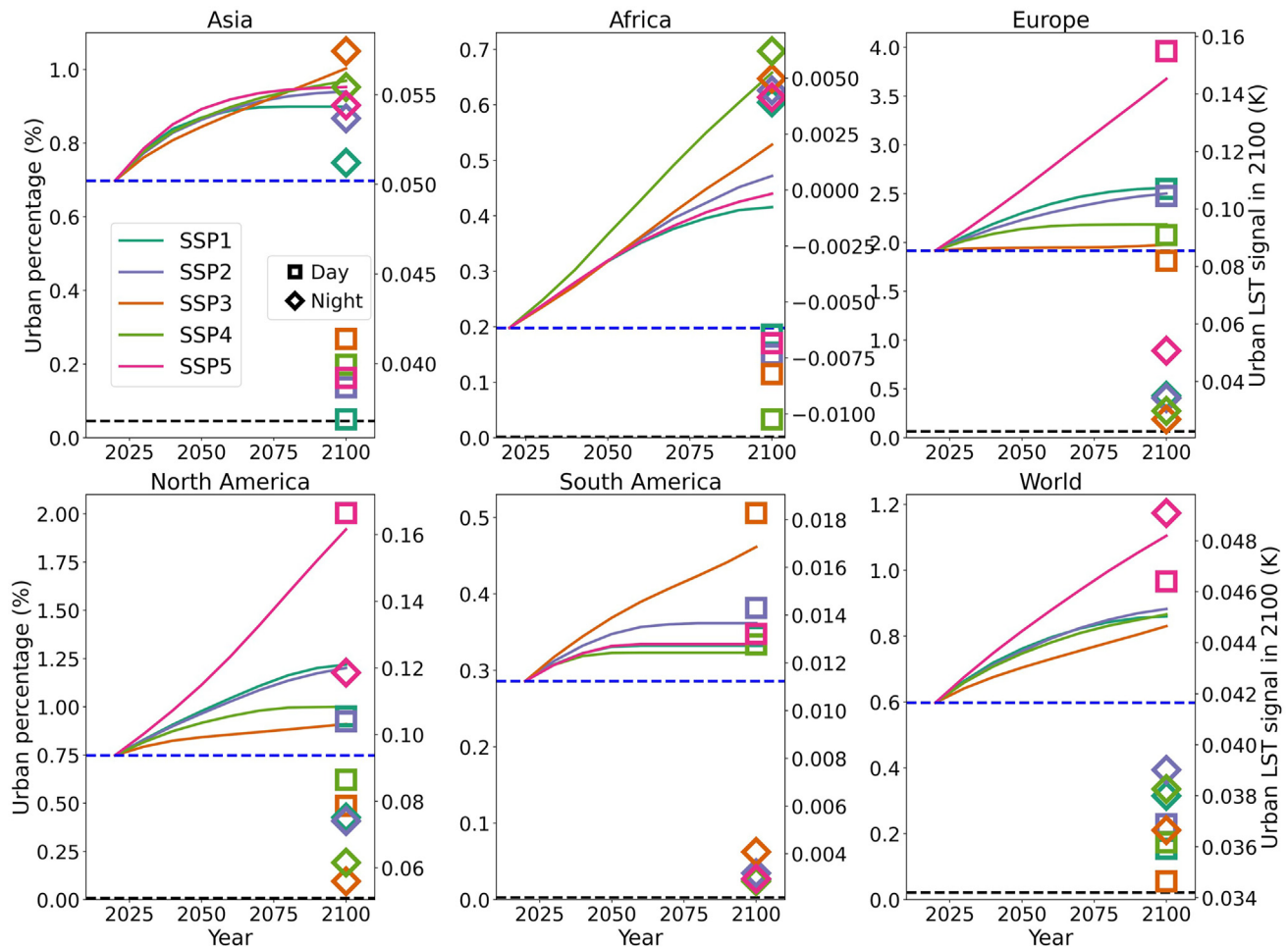
Figure 6. Urban temperature signal and urban percentages for SSPs
Urban percentage for different SSPs for the continents and the world based on 1-km global projections. In each case, the horizontal black and blue dashed lines represent estimated urban percentage for 1880 and 2019, respectively. The squares and diamonds (tick labels on the right-hand y axis), colored based on SSP scenarios, represent total daytime and nighttime urban LST signals for 2100.

expansion on regional climate (Figures 5 and 7). Moreover, other radiative constraints relevant to urbanization are also poorly represented, static, or both in commonly used numerical models.[4,50] In contrast, satellite observations suggest other clear continental-scale changes associated with urbanization (Figure 7). This includes increasing trends in the urban aerosol (except for Europe) and roughness (except for Africa) signals and decreasing trends in both the urban vegetation and α signal (except for South America). All of these ancillary changes over time are included and contribute to the urban LST signal, since it is from observations over global urban land over time. Based on permutation importance scores from fifty iterations of random Forest models (see experimental procedures), we find that, for daytime, the urban vegetation signal is most important for predicting the urban LST signal, while roughness is the most important at night (Figure S9). These changes can further influence regional and maybe even global climate through adjustments in the radiative budget, as well as through non-radiative feedback.[51] Of these, α modification through LULC change (LULCC) has been increasingly considered in global climate as-

sessments.[52] Based on the sensitivities of the urban α signal to urbanization (Figure 7B), the urban-induced change in global α since pre-industrial period is −0.00012, roughly one-tenth of the 0.00106 found for all LULCC.[53] Extrapolating these historical sensitivities for future scenarios will probably lead to overestimations of the urban contribution to LST and AT as α management strategies become more common in cities.

ESMs are now used not just for simulating global future climate, but also to test regional mitigation and adaptation scenarios.[54] For instance, the YRB, YRD, and IGB are expected to continue to urbanize in the future, with the YRB reaching 2.91% urban percentage in 2100 for SSP5, the YRD reaching 12.03%, and the IGB reaching 1.65%. At these scales, urbanization can have even greater contributions, with the fractional urban contribution to daytime LST reaching 0.31, with the potential for almost 0.4 K regional warming in 2100 for SSP5, using the YRD region as an example (Figure 4). That the sensitivities of the urban LST signal to urban percentage vary (and are sometimes opposite in sign) across these regions (Figures 4E–4G) illustrates the complexity of the urban influence on regional climate. Thus, we need to
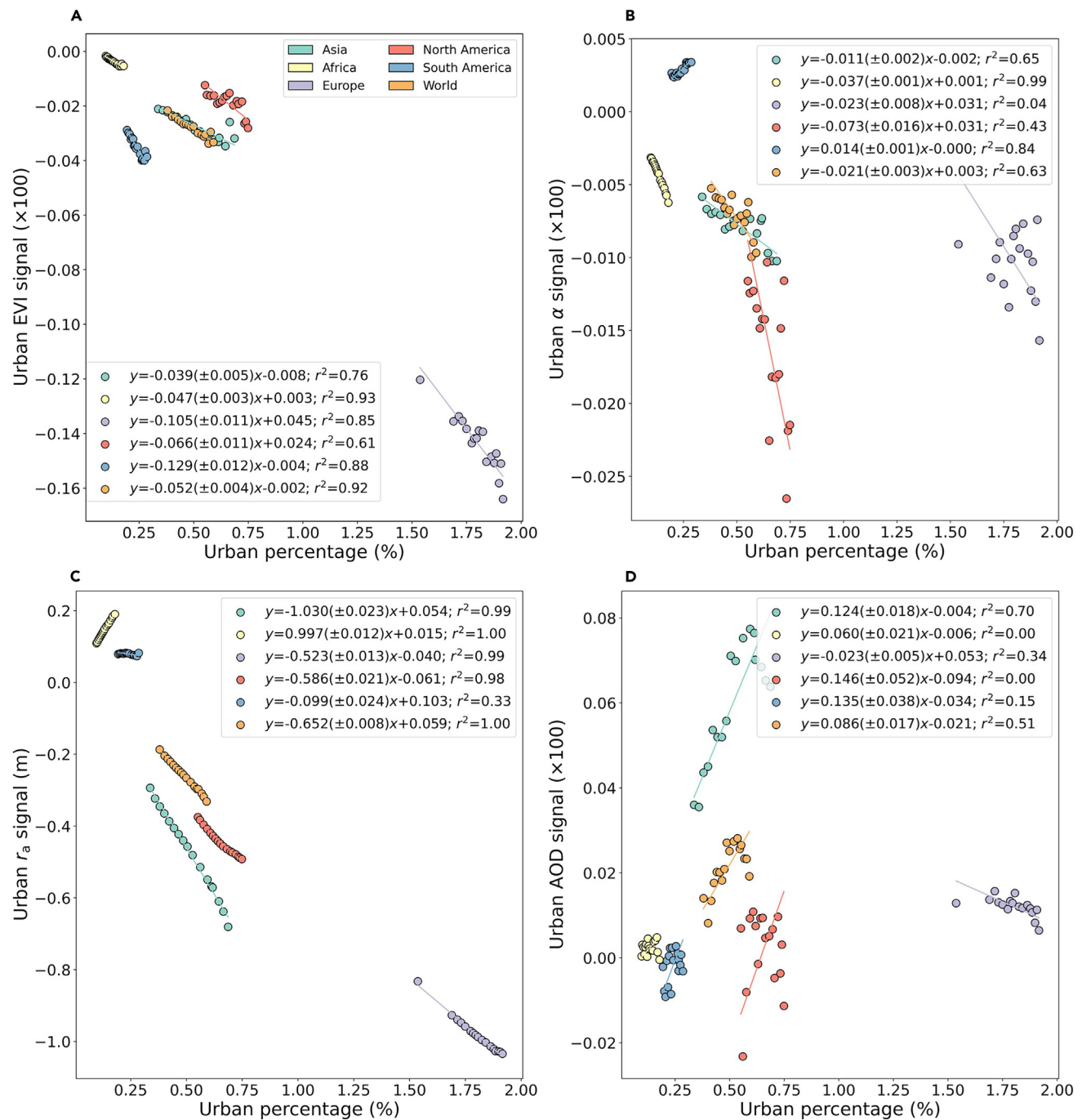
One Earth
Article

Figure 7. Associations between other surface and atmospheric urban signals and urban percentage

(A) Associations between the yearly (2003–2019) urban signal on the EVI and the corresponding urban percentage for continental and global scales.

(B–D) Similar to (A), but for surface albedo (α), a proxy for surface roughness (r_a), and AOD, respectively. The lines of best fit, including the standard errors of the slopes, and the coefficients of determination are noted for all cases. The EVI, α, and AOD signals are multiplied by 100 to limit the number of decimal points in the equations.

improve urban representation in ESMs to more accurately simulate regional climate.[22,55] Similar model improvements to incorporate land cover changes and land management practices are also being undertaken.[56] We currently have more than enough evidence to move past the debate on whether urbanization is

the reason for global warming trends. The warming has happened regardless of urbanization due to other anthropogenic changes to the Earth system,[57] with urbanization slightly adding to that warming. Apart from the urban-induced modifications shown in Figure 7, urbanization can also lead to complex regional feedback

on clouds and boundary layer,[29,58,59] which are difficult to assess at larger scales without accurately representing urban areas and their long-term dynamics in models. Although our statistical bulk sensitivities (Figure 5) are a compositive proxy for all these feedback for the recent past, we cannot say how the magnitude of the feedback will change in a warmer and wetter world[60] without process-based implementations. Importantly, in addition to overall urban expansion, there are multiple competing factors that need to be incorporated in dynamic urban representations in next-generation ESMs—from unique densification rates in cities that vary by region to changes in greening and α management strategies.[14,51] With the majority of the global population expected to live in cities in the future,[37] our results support the importance of explicitly treating urbanization (or preferably, "urban evolution") as another LULCC to capture a critical component of the Anthropocene.

EXPERIMENTAL PROCEDURES

Resource availability
Lead contact
Further information and requests for resources and materials should be directed to and will be fulfilled by the lead contact, TC Chakraborty (tc.chakraborty@pnnl.gov).
Materials availability
Materials generated in this study have been deposited on Zenodo: https://doi.org/10.5281/zenodo.11167731.
Data and code availability
The datasets generated for this study are all publicly archived on Zenodo: https://doi.org/10.5281/zenodo.11167731.

Country-wise urban area for different periods
The availability of long-term satellite observations enables spatially continuous estimates of urban area and its dynamic shifts at a global scale by leveraging the unique spectral signature of these surfaces.[19] This is generally more accurate than classifying urban and rural weather stations using either administrative boundaries, which do not necessarily correlate with physical urbanization or population thresholds,[37] which are poor proxies for the physical impacts of urbanization on local climate.[5,17]

For historical trends, we use the ESA CCI land cover data, which is available yearly from 1992 to 2020 at approximately 300 m resolution.[61] The area of the urban class for each country and each year, as recognized by the World Bank (Figure 1A), is calculated from this dataset on the Google Earth Engine cloud computing platform.[62] For the continental-scale analyses, we do not separately include the results for Oceania and other islands in the main discussion, but those countries are accounted for in the global estimates.

To estimate pre-industrial urban area, we process the urban pixels in the recent anthropogenic estimates of the History Database of the Global Environment (HYDE version 3.2) for 1850.[63] This dataset is available at a 5′ by 5′ spatial resolution from 10,000 Before Common Era to 2015 Common Era. Finally, for future projections of urban land, we use the recently developed approximately 1-km dataset of future urbanization for all five SSPs, as defined by the CMIP6.[64] SSP1 is the "sustainability" scenario, SSP2 is the "middle-of-the-road" scenario, SSP3 is the "regional rivalry" scenario, SSP4 is the "inequality" scenario, and SSP5 is the "high-emission" scenario.

Both the HYDE dataset and the future projections are calibrated against the ESA CCI data for present conditions according to the original methodologies,[63,64] lending consistency when combining them for the study. However, the baseline year used to calibrate the future projections in Chen et al.[64] against the ESA CCI data was 2015. Since that study, dynamic land cover data for 2016, 2017, 2019, and 2020 have become available. We found that the 2020 projections for even SSP1 from Chen et al.[64] were lower than the direct 2020 estimates from ESA CCI, especially over Asia and Europe (Figure S10A). So, we adjust the 2020 value for all SSP scenarios to be identical to the 2020 values at the continental and global scales. This adjustment

does not change our results much (increasing the daytime urban LST signal in 2100 for SSP5 scenario over Asia from 0.034 K to 0.039 K, for example), but does demonstrate the difficulty of projecting urban growth, especially over rapidly urbanizing regions.

Urban temperature signals at continental scales
We generate annual composites of LST from approximately 13,000 daily global MODIS observations.[32] The Aqua and Terra satellites, which carry the MODIS sensors, cross the equator at four times, at approximately 10:30 a.m. and approximately 10:30 p.m. local time (for Terra) and approximately 1:30 a.m. and approximately 1:30 p.m. local time (for Aqua). The overpass times are relatively stable for a pixel over the year, making it simple to generate composites corresponding with the overpass times. Complete global observations from these sensors are available starting from 2001 for Terra and 2003 for Aqua at approximately a 1-km resolution. The same MODIS sensors have continuously monitored the Earth throughout this period, unlike ground-based weather stations, for which sensor changes are common. Based on the quality-control flags in the derived product, we mask out pixels if the uncertainty is greater than 3 K before compositing.

The urban temperature signal (ΔLST_u) is calculated as the difference between spatially averaged (by country, continent, region, or all terrestrial surfaces) LST for all land pixels (LST_{all}) and the average LST for all but urban land pixels (LST_{all-u}) (Figures 2 and S3). Thus:

$$\Delta LST_u = LST_{all} - LST_{all-u}. \quad \text{(Equation 1)}$$

The water pixels are masked out in both cases. These masks are generated from the ESA CCI land cover data for the corresponding years (2003–2019 for Aqua and 2001–2019 for Terra). We do not include 2020 in this analysis, since that was not a typical year, with major lockdowns due to COVID-19 impacting urban climate signals.[65] The spatial averaging is done after re-gridding the MODIS composites to approximately a 300-m resolution, same as the ESA CCI data. Note that the overall LST trends result (Figure S3) from several competing factors, including changes in biophysical surface properties, inter-decadal to multi-decadal variability, long-term trends in solar brightening and dimming driven by cloud cover, aerosols, and other atmospheric constituents, and so on.[34,66,67] As an example, China and India, which have experienced significant urbanization and, thus, strong urban LST signals, show statistically insignificant or even negative changes in overall LST (Figures S5, and S6; also see Figure 4 for three rapidly urbanizing regions overlaying these countries). Part of this could be related to greening trends over these two countries during this period,[68] which is a negative feedback to surface warming. Similarly, large solar brightening trends have been seen over Europe,[34,69] which would explain the relatively large magnitudes of LST trends over this region (Figures 3A, 3D, and S3). In the present study, we do not focus on the contributors to these overall trends and, through Equation 1, remove the impact of these other factors to isolate the bulk urban signal. We also do not focus on local-scale urban climate signals, such as the UHI, which has been studied extensively in the past using satellite-derived or modeled surface temperature.[9–13,70] Observational studies also commonly account for elevation differences between urban and rural areas before isolating local urban climate signals. Although this is simple to incorporate into our workflow, we do not do this here for two reasons. First, because removing pixels using elevation thresholds is not consistent with our objective of estimating the urban signals averaged over all land surfaces. Second, the impacts of elevation should be minimal over time, and would generally cancel out when estimating the signals as functions of urbanization.

Overall, here we consider urbanization from a broader context, which includes both biophysical changes in surface properties (such as more built-up structures and replacement of vegetation),[10,12] but also their associated effects on atmospheric forcing (such as through aerosol loading[71]; see next subsection). The default daytime and nighttime warming estimates presented here refer to the LST corresponding to the Aqua overpass. LST from other satellites (Terra and Landsat), as well as AT, are also considered (and explicitly mentioned) for specific discussions.

Continental urban signals for other factors
In addition to LSTs, we also estimate the urban signal for other surface and atmospheric variables that are known to be modulated by urbanization.[9,10,51]

One Earth
Article

This includes proxies for surface vegetation and aerodynamic roughness, surface reflectivity of solar radiation, and air pollution. Note that, similar to the urban LST signal, these trends account for absolute changes in the variables due to regional factors not directly related to urbanization (including air pollution cleaning efforts, and large-scale deforestation/afforestation).

The enhanced vegetation index (EVI), a proxy for live vegetation on the surface, is used to estimate the urban signal on continental-scale vegetation. The EVI is used instead of the commonly used normalized difference vegetation index (NDVI), since the NDVI can get saturated over dense vegetation, such as over the tropics.[72] Similar to the LST, annual composites are created from 2003 to 2019 based on the cloud-screened 16-day MODIS-derived vegetation indices available at approximately 250-m resolution.[73] As expected, the continental-scale urban EVI signal decreases with continued urbanization, with the smallest decrease seen over Africa and the largest over South America (Figure 7A).

Aerodynamics roughness (r_a) is generally difficult to measure over heterogeneous terrain, particularly cities. Here, we approximate it as the standard deviation of the global ALOS World 3D - 30m (AW3D30) digital surface model.[74] This approximation has been used in past studies[13,75] and works reasonably at coarser scales. For instance, the urban r_a signal increases with urbanization in Africa and decreases everywhere else (Figure 7C). This is what one would expect; arid landscapes tend to be aerodynamically smoother than cities, while vegetation landscapes, more common over the other continents, are aerodynamically rougher.[10,66] Unfortunately, the AW3D30 data are not available yearly, which prevents detection of change in urban r_a over time.

The total reflectivity or albedo (α) at the surface can be separated into the black-sky albedo (BSA), or the reflectivity of the direct beam radiation, and the white-sky albedo (WSA), the reflectivity of diffuse radiation. Annual (2003–2019) composites of WSA and BSA are generated from the MODIS daily albedo product available at approximately 500-m resolution using the best-quality pixels using the quality-control flags.[76] Finally, these two composites are combined with annual pixel-wise estimates of diffuse fraction of sunlight (k_d) to get the total α:

$$\alpha = WSA\, k_d + BSA(1 - k_d). \quad \text{(Equation 2)}$$

There are large biases in k_d in most long-term reanalysis and satellite-derived products compared with observations.[69] So we instead extract k_d from the bias-adjusted RADiation dataset, which is generated using a supervised learning algorithm using a global observation network.[77] In all cases other than in South America, the urban α signal is negative, or urban areas are darker than natural surfaces.

Finally, we generate annual composites of aerosol optical depth (AOD), a measure of the bulk radiative properties of the aerosols in an atmospheric column, from the approximately 1-km daily MODIS product derived from measurements from Terra and Aqua using pixels with the higher quality-control flags.[78] As expected, in all continents, the urban AOD signal is positive, or urban areas raise the continental-scale averages by having heavier aerosol loading. The strongest signals are seen over North America (Figure 7D). Since the urban signal for EVI, α, and AOD can reach the fourth or fifth decimal places, we multiply these by 100 in Figure 7.

Trend and sensitivity analyses

To calculate the long-term trends, the overall country-wise averages (LST$_{all}$, and similarly EVI$_{all}$, $r_{a,all}$, α_{all}, and AOD$_{all}$) as well as the urban signals (ΔLST$_u$, ΔEVI$_u$, $\Delta r_{a,u}$, $\Delta \alpha_u$, and ΔAOD$_u$) are regressed against the year using ordinary least squares (OLS). Dividing the urban signals by the overall trends (say ΔLST$_u$/LST$_{all}$) provides a preliminary estimate for the urban contribution to the trends during the chosen time period. We stress that these trends, and thus these contributions, are reflective of the changes during that period and can be somewhat unstable, especially when the overall changes are close to zero. So, we also calculate the sensitivities of these urban signals to the urban percentages calculated from the ESA CCI data, which removes the explicit dependence on time. Similar sensitivities can also be estimated for specific seasons. For instance, see Figure S11 for estimates for summer day and night. These are derived from images for June, July, and August for the northern hemisphere and December, January, and February for the southern hemisphere. However, it should be noted that different climate zones have different

cloud cover percentages with distinct seasonality,[79] which would make it more uncertain to establish stable trends for smaller subsets of the year.

When calculating these sensitivities, since both x and y variables have errors, we use the reduced major axis regression,[80] instead of OLS regression. The slope of this regression can be combined with the calculated urban fractions (f_b) for the past and the future to estimate the corresponding urban signals for different periods. Below is an example for the total LST change due to urbanization between 1850 (pre-industrial) and 2100 for the SSP5 scenario (ΔLST$_{2100,SSP5-1850}$):

$$\Delta LST_{u,2100-1850} = \frac{\Delta LST_{u,std}}{f_{b,std}} (f_{u,2100,SSP5} - f_{u,1850}). \quad \text{(Equation 3)}$$

Here, $\frac{\Delta LST_{u,std}}{f_{b,std}}$ is the slope of the reduced major axis regression based on the standard deviations ($_{std}$) of the two variables between 2003 and 2019, $f_{b,2100,SSP5}$ is the urban fraction based on the adjusted future projections of urbanization and $f_{b,1850}$ is the urban fraction for 1850 from the HYDE dataset.

Regional trends for rapidly urbanizing regions

Our method (Equation 1) is a function of both the overall regional trend and the regional trend without considering the urban pixels. As such, unique regional urban LST signals would emerge that would have distinct degrees of relevance to human impacts depending on regional population density. For instance, removing the Sahara Desert alters the sensitivity of the urban LST signal over Africa to changes in urbanization, while still maintaining the same direction of the urban contribution (Figure S12). We also illustrate the urban contribution to LST trends for three rapidly urbanizing and densely populated regions in Asia—the YRB, the YRD, and the IGB.

Distinction of our approach from traditional methods

In the satellite remote-sensing literature, urban impacts on warming are almost always quantified at the local scale,[11,15,30] usually by subtracting the mean urban LST from the LST of a neighboring region, also called the rural reference.[31] This is because, at larger scales, urban and non-urban regions are unevenly distributed and can be in very different climate zones. For instance, there is a concentration of urban areas in coastal environments,[81] which have unique climatic patterns and interactions with urbanization.[82] By using a rural reference close to, and generally surrounding the urban area, the sampling bias of urban areas in larger regions can be eliminated. However, our goal here is not to examine this local-scale urban signal, also called the surface UHI which has been extensively studied in the past.[15,30,50] Instead, we wanted to estimate if the urban impact on temperature can be detected at larger scales (regional to continental) regardless of the distribution of urban areas in those regions. This is important both for understanding whether urbanization can have a detectible impact on large-scale climatological signals[17,20,21] and for supporting the need for explicit representation of urban areas in Earth system and climate models.[49,55]

To illustrate, we compare our approach to a traditional buffer-based method, often used to estimate the surface UHI intensity. We first vectorize contiguous groups of urban pixels in the 2019 estimate of the ESA CCI dataset. This generates 846,742 urban clusters globally. To ensure a clean urban signal at the MODIS LST scale, we only consider the clusters that are larger than 1 km^2, which leaves 83,102 clusters. Then, we use an interactive approach to create buffered regions around each urban cluster, such that the buffer is roughly equal in area to the urban cluster it surrounds. The surface UHI is then calculated as the difference in average LST of the urban clusters and the average LST of the non-urban and non-water pixels within the rural references (buffers) of those clusters. Similar normalized buffer approaches are common in the literature.[31,65] As one might expect, the local urban LST signal, or the surface UHI, shows much higher values for all continents than the urban LST signal at the continental/global scale (Figure S13).

Contributions of factors to urban temperature signal

Although not the primary focus of the study, we also examine the associations between the country-scale urban LST signal and the corresponding signals for major surface and atmospheric factors as a sanity check. To do this, we first calculate all the trends in the urban signals between 2003 and 2019 and treat the trend for each country as a sample. To capture both linear and non-linear

interactions, we use RF regression, which is a non-parametric machine learning technique that uses ensembles of weak learners (decision trees) and is less sensitive to outliers than parametric models.[83] Similar methods have been used in previous studies on local warming due to urbanization.[13,65] The RF models represent the trend in ΔLST_u ($\Delta LST_{u,t}$) as generic functions of the corresponding trends in ΔEVI_u, $\Delta r_{a,\,u}$, $\Delta \alpha_u$, and ΔAOD_u. Thus:

$$\Delta LST_{u,t} = f(\Delta EVI_{u,t}, \Delta r_{a,u,t}, \Delta \alpha_{u,t}, \Delta AOD_{u,t}) \qquad \text{. (Equation 4)}$$

To examine consistency of the results, the RF models are run using all samples (countries) a total of 50 times using default hyperparameters and out-of-bag (OOB) score estimation turned on using the scikit-learn Python package. Normally, machine learning models require separate training and validation data with different random splits to reduce dependence on the choice of the training subset. However, with bootstrapping turned on, RF models internally choose a random subset of the dataset for each iteration. The OOB validation gives us the accuracy of the model for the subset of data not used for training for each of those iterations. Finally, we calculate permutation importance scores for each feature, which give us the relative importance of a feature in the model by randomly shuffling them and estimating changes in the model score. Overall, the average OOB validation r^2 from all 50 runs is around 0.40 during daytime and 0.11 at night. This suggests that we are still missing some key features, particularly at night, which makes sense when contextualized within the existing literature.[9] Many of these additional features cannot be derived at these scales using satellites. Moreover, while the RF models give us associations as learned from the distribution in the training data, they cannot establish causality. For instance, several of these variables (such as EVI and α) are correlated.[65] This reinforces the need for process-based models that can represent urban-scale interactions and their changes over time and thus allow more targeted modeling experiments for future scenarios of urbanization and their possible larger scale feedback. According to the permutation scores, during daytime, $\Delta EVI_{u,\,t}$ is the most important variable, while $\Delta r_{a,\,u}$ becomes more important at night, which is generally consistent with a previous urban-scale estimate.[13]

Verifying results across regions, periods, and datasets

In the present study, we use countries as the common geographic units of calculation since many of these results are nationally relevant and these estimates can be easily aggregated to the continental scale. The methods of the present study can be used for any region, as seen from the regional analysis earlier. To illustrate the presence of similar larger scale trends for more climate-relevant regions of interest, we recalculate the sensitivities of the urban LST signal from the MODIS Aqua observations using the Köppen-Geiger climate zones[84]—namely tropical, arid, temperate, boreal, and polar—as the geographic units of calculation. As expected, consistent urban warming signals linearly associated with urbanization are seen in all cases other than for Arid climate zone during daytime (Figure S14). The urban cooling signal is consistent with the generally negative daytime surface UHI in arid areas[10,11] and also with the results seen for Africa (Figure 5A).

One limitation of the present study is the relatively short time series for the MODIS observations, which is why there is a disconnection between the analysis of urban expansion for 1992 to 2019, and for the rest of the analysis (2003–2019). Note that this latter period also shows rapid urbanization (Figure S2). Estimates of LST from the Landsat satellites, with native resolution of approximately 60 m for Landsat 7 to approximately 120 m for Landsat 5 (approximately 100 m for Landsat 8), can be an alternative here due to the longer time series.[33] We calculate similar urban LST signals from the Landsat collection 2 product using the ESA CCI dataset for both the 2003–2019 period (Landsat_ESA in Figures 5C and 5D) and for the entire ESA CCI archive (1992–2019; Landsat_ESA_1992 in Figures 5C and 5D). Pixel-level quality control flags are used before generating annual means. Landsat 5 data are used for 1992–2011 (1,402,063 images used), Landsat 7 for 2013 and 2014 (218,227 images used), and Landsat 8 from 2015 onwards (928,993 images used). The sensitivities are consistent for both time periods when compared with the MODIS-derived daytime estimates from Terra (closest overpass time to Landsat) globally and across continents (Figures 5C and 5D). Since the timing and rate of urbanization varies across continents, we also check whether the urban LST signals are consistently seen for different subsets of

this 1992–2019 period. We do so by calculating trends for all consecutives 17-year periods, which equals the length of the time series used for the MODIS Aqua analysis in the main text, from the Landsat estimates. Consistent positive LST signals are found for all continents other than Africa for all the subperiods (Figure S15). Of note, North America shows stronger sensitivity of the urban LST signal to urban percentage in second one-half of the subperiods while the opposite is true for South America. For Africa, the negative sensitivities tend to get less negative in more recent subperiods, suggesting changes in the urbanization regime in Africa in more recent years. However, we should note that the Landsat measurements have several limitations for the purposes of this study. These limitations include very few nighttime overpasses, thus only allowing daytime estimates, a 16-day return period (vs. daily for MODIS), making the data more susceptible to cloud contamination when estimating annual means, changes in sensors during the study period, unequal coverage across continents, and a lack of standardization for prescribing surface emissivity, particularly an issue over urban areas.[50]

A second source of uncertainty is the choice of urban dataset, both for historical land cover and for future projections. We use the ESA CCI data as the default land cover in our analysis due its consistency with the historical HYDE data as well as the future projections from Chen et al.,[64] overall ability to pick up urban growth over time,[85] and similar resolution to the MODIS LST data. To confirm the presence and magnitude of this urban LST signal's sensitivity to urbanization, we consider two additional annual land cover datasets, namely the MODIS land cover version 6, available at 500-m resolution from 2001 to present,[85] and the global artificial impervious area dataset,[86] available at 30-m resolution from 1985 to 2018. Using the Aqua estimates (approximately 1:30 a.m. and approximately 1:30 p.m. local time) as the standard for comparison, we similarly calculate the urban LST signal (Equation 1) after regridding the LST data to the native resolution of the land cover dataset. The other datasets also show similar sign of the sensitivity (except for Europe at nighttime) and generally similar rank of sensitivities across continents. However, we do note much higher sensitivities from the MODIS data. This is because the MODIS land cover dataset barely shows any long-term changes in urban area compared with other datasets (Figure S1) (also see Huang et al.[85]), thus increasing the sensitivity of the urban LST signal to unit changes in urban percentage. Similarly, for future urbanization, using a different projection,[87] we find much larger urban contribution to continental and global land LST (Figure S7). As an illustration, the daytime urban LST signal over Asia at the end of the century for SSP5 scenario is 0.039 K based on Chen et al.[64] and over three times that (0.136 K) based on Gao and O'Neill.[87] The projections from Gao and O'Neill[87] suggest much more urbanization in the future (e.g., 2–2.5 times the estimates from Chen et al.[64] at the end of the century). This is due to different assumptions about the SSP scenarios used when generating the datasets, consideration of different number of sub-regions (32 in Chen et al.[64] versus 375 in Gao and O'Neill[87]), and differences in how the datasets are calibrated. This leads to some interesting regional differences, with the Chen et al.[64] dataset not showing much divergence for the different SSP scenarios over Asia compared with the projections from Gao and O'Neill.[87] In summary, although different historical estimates and future projections of urbanization would lead to different magnitudes of the urban warming signal, the signal itself is consistent across datasets.

Satellite observations have missing data due to cloud contamination, shadows, and other atmospheric interferences. To test how these missing pixels affect our results, we recalculate the sensitivities of urban LST signal to urban percentage using a recently released approximately 1-km seamless daily LST product generated using MODIS Terra and Aqua observations and a comprehensive gap-filling procedure.[88] These sensitivities (Figure S16) are practically identical to those seen in Figure 3 based on the 2003–2019 period. Thus, the missing data have very little effect on long-term changes in the urban LST, and thus estimates of future urban contribution to continental-scale LST change. Regardless of the gap-filling method used, the LST data are valid for clear-sky conditions, while weather stations can measure ambient AT even when there are clouds. However, it is difficult to justify that there is no urban contribution to continental-scale temperature for all-sky conditions when the clear-sky signals are so clear.

Finally, LST is not AT and the two can be poorly coupled spatially within and across urban areas.[13] However, this coupling is expected to be stronger at the annual scale and especially when looking at larger regions. To confirm, we

One Earth
Article

calculate sensitivities in maximum and minimum annual average urban AT signal based on a recent daily 1-km dataset.[89] Overall, clear urban AT signals are seen with similar ranking of magnitudes across continents for both daytime and nighttime (Figure S8). The sensitivities for AT tend to be lower than that for LST, although the degree of uncoupling varies by continent (Figures 3A, 3B, S8A, and S8B). While we do not examine this here, we would expect the degree of decoupling to also vary by season. We stress here that these clear urban AT signals should be contextualized against the existing studies that commonly use weather station data[16–18,22] and is important for understanding regional heat exposure beyond the urban boundary. In contrast, the somewhat stronger urban LST signals are more relevant for climate-related feedback due to the lower boundary constraints provided by LST on near-surface and atmospheric processes.

SUPPLEMENTAL INFORMATION

Supplemental information can be found online at https://doi.org/10.1016/j.oneear.2024.05.005.

ACKNOWLEDGMENTS

AUTHOR CONTRIBUTIONS

T.C. designed the study, processed the satellite observations, analyzed the data, and wrote the first draft of the manuscript. Y.Q. provided additional inputs on concept, methodology, and writing.

DECLARATION OF INTERESTS

The authors declare no competing interests.

REFERENCES

1. Feddema, J.J., Oleson, K.W., Bonan, G.B., Mearns, L.O., Buja, L.E., Meehl, G.A., and Washington, W.M. (2005). The Importance of Land-Cover Change in Simulating Future Climates. Science 310, 1674–1678. https://doi.org/10.1126/science.1118160.

2. Luyssaert, S., Jammet, M., Stoy, P.C., Estel, S., Pongratz, J., Ceschia, E., Churkina, G., Don, A., Erb, K., Ferlicoq, M., et al. (2014). Land management and land-cover change have impacts of similar magnitude on surface temperature. Nat. Clim. Chang. 4, 389–393. https://doi.org/10.1038/nclimate2196.

3. Lawrence, D.M., Hurtt, G.C., Arneth, A., Brovkin, V., Calvin, K.V., Jones, A.D., Jones, C.D., Lawrence, P.J., de Noblet-Ducoudré, N., Pongratz, J., et al. (2016). The Land Use Model Intercomparison Project (LUMIP) contribution to CMIP6:rationale and experimental design. Geosci. Model Dev. (GMD) 9, 2973–2998. https://doi.org/10.5194/gmd-9-2973-2016.

4. Zheng, Z., Zhao, L., and Oleson, K.W. (2021). Large model structural uncertainty in global projections of urban heat waves. Nat. Commun. 12, 3736–3739.

5. Peterson, T.C. (2003). Assessment of Urban Versus Rural In Situ Surface Temperatures in the Contiguous United States: No Difference Found. J. Clim. 16, 2941–2959. https://doi.org/10.1175/1520-0442(2003)016<2941:AOUVRI>2.0.CO;2.

6. Parker, D.E. (2006). A Demonstration That Large-Scale Warming Is Not Urban. J. Clim. 19, 2882–2895. https://doi.org/10.1175/JCLI3730.1.

7. Wang, F., Ge, Q., Wang, S., Li, Q., and Jones, P.D. (2015). A new estimation of urbanization's contribution to the warming trend in China. J. Clim. 28, 8923–8938.

8. Sharma, A., Wuebbles, D.J., Kotamarthi, R., Calvin, K., Drewniak, B., Catlett, C.E., and Jacob, R. (2020). Urban-Scale Processes in High-Spatial-Resolution Earth System Models. Bull. Am. Meteorol. Soc. 101, E1555–E1561. https://doi.org/10.1175/BAMS-D-20-0114.1.

9. Arnfield, A.J. (2003). Two decades of urban climate research: a review of turbulence, exchanges of energy and water, and the urban heat island. Int. J. Climatol. 23, 1–26.

10. Zhao, L., Lee, X., Smith, R.B., and Oleson, K. (2014). Strong contributions of local background climate to urban heat islands. Nature 511, 216–219.

11. Chakraborty, T., and Lee, X. (2019). A simplified urban-extent algorithm to characterize surface urban heat islands on a global scale and examine vegetation control on their spatiotemporal variability. Int. J. Appl. Earth Obs. Geoinf. 74, 269–280. https://doi.org/10.1016/j.jag.2018.09.015.

12. Manoli, G., Fatichi, S., Schläpfer, M., Yu, K., Crowther, T.W., Meili, N., Burlando, P., Katul, G.G., and Bou-Zeid, E. (2019). Magnitude of urban heat islands largely explained by climate and population. Nature 573, 55–60. https://doi.org/10.1038/s41586-019-1512-9.

13. Venter, Z.S., Chakraborty, T., and Lee, X. (2021). Crowdsourced air temperatures contrast satellite measures of the urban heat island and its mechanisms. Sci. Adv. 7, eabb9569. https://doi.org/10.1126/sciadv.abb9569.

14. Liu, Z., Zhan, W., Bechtel, B., Voogt, J., Lai, J., Chakraborty, T., Wang, Z.-H., Li, M., Huang, F., and Lee, X. (2022). Surface warming in global cities is substantially more rapid than in rural background areas. Commun. Earth Environ. 3, 219.

15. Clinton, N., and Gong, P. (2013). MODIS detected surface urban heat islands and sinks: Global locations and controls. Remote Sens. Environ. 134, 294–304. https://doi.org/10.1016/j.rse.2013.03.008.

16. Kalnay, E., and Cai, M. (2003). Impact of urbanization and land-use change on climate. Nature 423, 528–531.

17. Zhang, P., Ren, G., Qin, Y., Zhai, Y., Zhai, T., Tysa, S.K., Xue, X., Yang, G., and Sun, X. (2021). Urbanization Effects on Estimates of Global Trends in Mean and Extreme Air Temperature. J. Clim. 34, 1923–1945. https://doi.org/10.1175/JCLI-D-20-0389.1.

18. Zhou, L., Dickinson, R.E., Tian, Y., Fang, J., Li, Q., Kaufmann, R.K., Tucker, C.J., and Myneni, R.B. (2004). Evidence for a significant urbanization effect on climate in China. Proc. Natl. Acad. Sci. 101, 9540–9544. https://doi.org/10.1073/pnas.0400357101.

19. Tysa, S.K., Ren, G., Qin, Y., Zhang, P., Ren, Y., Jia, W., and Wen, K. (2019). Urbanization effect in regional temperature series based on a remote sensing classification scheme of stations. JGR. Atmospheres 124, 10646–10661.

20. Hausfather, Z., Menne, M.J., Williams, C.N., Masters, T., Broberg, R., and Jones, D. (2013). Quantifying the effect of urbanization on US Historical Climatology Network temperature records. JGR. Atmospheres 118, 481–494.

21. Wickham, C., Rohde, R., Muller, R.A., Wurtele, J., Curry, J., Groom, D., Jacobsen, R., Perlmutter, S., Rosenfeld, A., and Mosher, S. (2013). Influence of Urban Heating on the Global Temperature Land Average using Rural Sites Identified from MODIS Classifications. Geoinfor Geostat: An Overview 1: 2. of 6, 1895–2007.

22. Ren, G., and Zhou, Y. (2014). Urbanization Effect on Trends of Extreme Temperature Indices of National Stations over Mainland China, 1961–2008. J. Clim. 27, 2340–2360. https://doi.org/10.1175/JCLI-D-13-00393.1.

23. Sun, Y., Zhang, X., Ren, G., Zwiers, F.W., and Hu, T. (2016). Contribution of urbanization to warming in China. Nat. Clim. Chang. 6, 706–709.

24. Muller, C.L., Chapman, L., Grimmond, C.S.B., Young, D.T., and Cai, X. (2013). Sensors and the city: a review of urban meteorological networks. Int. J. Climatol. *33*, 1585–1600. https://doi.org/10.1002/joc.3678.

25. Parker, D.E. (2010). Urban heat island effects on estimates of observed climate change. Wiley Interdiscip. Rev. Clim. Change *1*, 123–133.

26. Li, J., Zhan, W., Chakraborty, T.C., Liu, Z., Du, H., Liao, W., Luo, M., Li, L., Miao, S., Fu, H., et al. (2023). Satellite-Based Ranking of the World's Hottest and Coldest Cities Reveals Inequitable Distribution of Temperature Extremes. Bull. Am. Meteorol. Soc. *104*, E1268–E1281.

27. Georgescu, M., Moustaoui, M., Mahalov, A., and Dudhia, J. (2013). Summer-time climate impacts of projected megapolitan expansion in Arizona. Nat. Clim. Chang. *3*, 37–41.

28. Krayenhoff, E.S., Moustaoui, M., Broadbent, A.M., Gupta, V., and Georgescu, M. (2018). Diurnal interaction between urban expansion, climate change and adaptation in US cities. Nat. Clim. Chang. *8*, 1097–1103. https://doi.org/10.1038/s41558-018-0320-9.

29. Qian, Y., Chakraborty, T.C., Li, J., Li, D., He, C., Sarangi, C., Chen, F., Yang, X., and Leung, L.R. (2022). Urbanization Impact on Regional Climate and Extreme Weather: Current Understanding, Uncertainties, and Future Research Directions. Adv. Atmos. Sci. *39*, 819–860. https://doi.org/10.1007/s00376-021-1371-9.

30. Chen, G., Zhou, Y., Voogt, J.A., and Stokes, E.C. (2024). Remote sensing of diverse urban environments: From the single city to multiple cities. Remote Sens. Environ. *305*, 114108.

31. Yang, Q., Xu, Y., Tong, X., Huang, X., Liu, Y., Chakraborty, T.C., Xiao, C., and Hu, T. (2023). An adaptive synchronous extraction (ASE) method for estimating intensity and footprint of surface urban heat islands: A case study of 254 North American cities. Remote Sens. Environ. *297*, 113777.

32. Wan, Z. (2006). MODIS land surface temperature products users' guide. Inst. Comput. Earth Syst. Sci. Univ. Calif. St. Barbara CA USA *805*.

33. Loveland, T.R., and Dwyer, J.L. (2012). Landsat: Building a strong future. Remote Sens. Environ. *122*, 22–29.

34. Schwarz, M., Folini, D., Yang, S., Allan, R.P., and Wild, M. (2020). Changes in atmospheric shortwave absorption as important driver of dimming and brightening. Nat. Geosci. *13*, 110–115. https://doi.org/10.1038/s41561-019-0528-y.

35. Zhong, S., Qian, Y., Zhao, C., Leung, R., Wang, H., Yang, B., Fan, J., Yan, H., Yang, X.-Q., and Liu, D. (2017). Urbanization-induced urban heat island and aerosol effects on climate extremes in the Yangtze River Delta region of China. Atmos. Chem. Phys. *17*, 5439–5457. https://doi.org/10.5194/acp-17-5439-2017.

36. Zhou, D., Zhao, S., Zhang, L., Sun, G., and Liu, Y. (2015). The footprint of urban heat island effect in China. Sci. Rep. *5*, 11160.

37. Heilig, G.K. (2014). World Urbanization Prospects the 2014 Revision. U. N. Dep. Econ. Soc. Aff. DESA Popul. Div. Popul. Estim. Proj. Sect. N. Y..

38. Pörtner, H.-O., Roberts, D.C., Adams, H., Adler, C., Aldunce, P., Ali, E., Begum, R.A., Betts, R., Kerr, R.B., and Biesbroek, R. (2022). Climate change 2022: Impacts, adaptation and vulnerability. IPCC Sixth Assess. Rep.

39. NOAA National Centers for Environmental information (2021). Climate at a Glance: Global Time Series. https://www.ncdc.noaa.gov/cag/.

40. Garratt, J.R. (1995). Observed screen (air) and GCM surface/screen temperatures: Implications for outgoing longwave fluxes at the surface. J. Clim. *8*, 1360–1368.

41. Easterling, D.R., Horton, B., Jones, P.D., Peterson, T.C., Karl, T.R., Parker, D.E., Salinger, M.J., Razuvayev, V., Plummer, N., Jamason, P., and Folland, C.K. (1997). Maximum and Minimum Temperature Trends for the Globe. Science *277*, 364–367. https://doi.org/10.1126/science.277.5324.364.

42. Cox, D.T.C., Maclean, I.M.D., Gardner, A.S., and Gaston, K.J. (2020). Global variation in diurnal asymmetry in temperature, cloud cover, specific humidity and precipitation and its association with leaf area index. Glob. Chang. Biol. *26*, 7099–7111. https://doi.org/10.1111/gcb.15336.

43. Zhang, D.-L., Shou, Y.-X., Dickerson, R.R., and Chen, F. (2011). Impact of upstream urbanization on the urban heat island effects along the Washington–Baltimore corridor. J. Appl. Meteorol. Climatol. *50*, 2012–2029.

44. Zhou, D., Xiao, J., Frolking, S., Zhang, L., and Zhou, G. (2022). Urbanization contributes little to global warming but substantially intensifies local and regional land surface warming. Earth's Future *10*, e2021EF002401.

45. Jacobson, M.Z., and Ten Hoeve, J.E. (2012). Effects of Urban Surfaces and White Roofs on Global and Regional Climate. J. Clim. *25*, 1028–1044. https://doi.org/10.1175/JCLI-D-11-00032.1.

46. Oleson, K.W., and Feddema, J. (2020). Parameterization and surface data improvements and new capabilities for the Community Land Model Urban (CLMU). J. Adv. Model. Earth Syst. *12*, e2018MS001586.

47. Walters, D., Baran, A.J., Boutle, I., Brooks, M., Earnshaw, P., Edwards, J., Furtado, K., Hill, P., Lock, A., Manners, J., et al. (2019). The Met Office Unified Model global atmosphere 7.0/7.1 and JULES global land 7.0 configurations. Geosci. Model Dev. (GMD) *12*, 1909–1963.

48. Fischer, E.M., Oleson, K.W., and Lawrence, D.M. (2012). Contrasting urban and rural heat stress responses to climate change. Geophys. Res. Lett. *39*.

49. Zhao, L., Oleson, K., Bou-Zeid, E., Krayenhoff, E.S., Bray, A., Zhu, Q., Zheng, Z., Chen, C., and Oppenheimer, M. (2021). Global multi-model projections of local urban climates. Nat. Clim. Chang. *11*, 152–157.

50. Chakraborty, T.C., Lee, X., Ermida, S., and Zhan, W. (2021). On the land emissivity assumption and Landsat-derived surface urban heat islands: A global analysis. Remote Sens. Environ. *265*, 112682.

51. Ouyang, Z., Sciusco, P., Jiao, T., Feron, S., Lei, C., Li, F., John, R., Fan, P., Li, X., Williams, C.A., et al. (2022). Albedo changes caused by future urbanization contribute to global warming. Nat. Commun. *13*, 3800–3809.

52. Shukla, P.R., Skea, J., Calvo Buendia, E., Masson-Delmotte, V., Pörtner, H.O., Roberts, D.C., Zhai, P., Slade, R., Connors, S., and Van Diemen, R. (2019). IPCC, 2019: Climate Change and Land: an IPCC special report on climate change, desertification, land degradation, sustainable land management. Food Security, and Greenhouse Gas Fluxes in Terrestrial Ecosystems.

53. Ghimire, B., Williams, C.A., Masek, J., Gao, F., Wang, Z., Schaaf, C., and He, T. (2014). Global albedo change and radiative cooling from anthropogenic land cover change, 1700 to 2005 based on MODIS, land use harmonization, radiative kernels, and reanalysis. Geophys. Res. Lett. *41*, 9087–9096.

54. Kawamiya, M., Hajima, T., Tachiiri, K., Watanabe, S., and Yokohata, T. (2020). Two decades of Earth system modeling with an emphasis on Model for Interdisciplinary Research on Climate (MIROC). Prog. Earth Planet. Sci. *7*, 64. https://doi.org/10.1186/s40645-020-00369-5.

55. Sharma, A., Wuebbles, D.J., and Kotamarthi, R. (2021). The Need for Urban-Resolving Climate Modeling Across Scales. AGU Adv *2*. https://doi.org/10.1029/2020AV000271.

56. Pongratz, J., Dolman, H., Don, A., Erb, K.H., Fuchs, R., Herold, M., Jones, C., Kuemmerle, T., Luyssaert, S., Meyfroidt, P., and Naudts, K. (2018). Models meet data: Challenges and opportunities in implementing land management in Earth system models. Glob. Chang. Biol. *24*, 1470–1487. https://doi.org/10.1111/gcb.13988.

57. Lynas, M., Houlton, B.Z., and Perry, S. (2021). Greater than 99% consensus on human caused climate change in the peer-reviewed scientific literature. Environ. Res. Lett. *16*, 114005.

58. Theeuwes, N.E., Barlow, J.F., Teuling, A.J., Grimmond, C.S.B., and Kotthaus, S. (2019). Persistent cloud cover over mega-cities linked to surface heat release. npj Clim. Atmos. Sci. *2*, 15–16.

59. Petäjä, T., Järvi, L., Kerminen, V.-M., Ding, A.J., Sun, J.N., Nie, W., Kujansuu, J., Virkkula, A., Yang, X., and Fu, C.B. (2016). Enhanced air pollution via aerosol-boundary layer feedback in China. Sci. Rep. *6*, 1–6.

60. Wang, W., Chakraborty, T.C., Xiao, W., and Lee, X. (2021). Ocean surface energy balance allows a constraint on the sensitivity of precipitation to

global warming. Nat. Commun. *12*, 2115. https://doi.org/10.1038/s41467-021-22406-7.

61. Bontemps, S., Defourny, P., Radoux, J., Van Bogaert, E., Lamarche, C., Achard, F., Mayaux, P., Boettcher, M., Brockmann, C., and Kirches, G. (2013). Consistent global land cover maps for climate modelling communities: current achievements of the ESA's land cover CCI. In Proceedings of the ESA living planet symposium (Edimburgh: ESA), pp. 9–13.

62. Gorelick, N., Hancher, M., Dixon, M., Ilyushchenko, S., Thau, D., and Moore, R. (2017). Google Earth Engine: Planetary-scale geospatial analysis for everyone. Remote Sens. Environ. *202*, 18–27. https://doi.org/10.1016/j.rse.2017.06.031.

63. Klein Goldewijk, K., Beusen, A., Doelman, J., and Stehfest, E. (2017). Anthropogenic land use estimates for the Holocene – HYDE 3.2. Earth Syst. Sci. Data *9*, 927–953. https://doi.org/10.5194/essd-9-927-2017.

64. Chen, G., Li, X., Liu, X., Chen, Y., Liang, X., Leng, J., Xu, X., Liao, W., Qiu, Y., Wu, Q., and Huang, K. (2020). Global projections of future urban land expansion under shared socioeconomic pathways. Nat. Commun. *11*, 537. https://doi.org/10.1038/s41467-020-14386-x.

65. Chakraborty, T., Sarangi, C., and Lee, X. (2021). Reduction in human activity can enhance the urban heat island: insights from the COVID-19 lockdown. Environ. Res. Lett *16*, 054060.

66. Chakraborty, T., and Lee, X. (2019). Land cover regulates the spatial variability of temperature response to the direct radiative effect of aerosols. Geophys. Res. Lett. *46*, 8995–9003.

67. Naudts, K., Chen, Y., McGrath, M.J., Ryder, J., Valade, A., Otto, J., and Luyssaert, S. (2016). Europe's forest management did not mitigate climate warming. Science *351*, 597–600. https://doi.org/10.1126/science.aad7270.

68. Chen, C., Park, T., Wang, X., Piao, S., Xu, B., Chaturvedi, R.K., Fuchs, R., Brovkin, V., Ciais, P., Fensholt, R., et al. (2019). China and India lead in greening of the world through land-use management. Nat. Sustain. *2*, 122–129. https://doi.org/10.1038/s41893-019-0220-7.

69. Chakraborty, T., and Lee, X. (2021). Large Differences in Diffuse Solar Radiation Among Current-Generation Reanalysis and Satellite-Derived Products. J. Clim. *34*, 6635–6650.

70. Ren, G.-Y. (2015). Urbanization as a major driver of urban climate change. Adv. Clim. Change Res. *6*, 1–6. https://doi.org/10.1016/j.accre.2015.08.003.

71. Cao, C., Lee, X., Liu, S., Schultz, N., Xiao, W., Zhang, M., and Zhao, L. (2016). Urban heat islands in China enhanced by haze pollution. Nat. Commun. *7*, 12509. https://doi.org/10.1038/ncomms12509.

72. Huete, A., Didan, K., Miura, T., Rodriguez, E.P., Gao, X., and Ferreira, L.G. (2002). Overview of the radiometric and biophysical performance of the MODIS vegetation indices. Remote Sens. Environ. *83*, 195–213.

73. Huete, A., Justice, C., and Van Leeuwen, W. (1999). MODIS vegetation index (MOD13). Algorithm Theor. Basis Doc. *3*, 295–309.

74. Takaku, J., Tadono, T., and Tsutsui, K. (2014). GENERATION OF HIGH RESOLUTION GLOBAL DSM FROM ALOS PRISM. ISPRS Ann. Photogramm. Remote Sens. Spat. Inf. Sci. *2*.

75. Glenn, N.F., Streutker, D.R., Chadwick, D.J., Thackray, G.D., and Dorsch, S.J. (2006). Analysis of LiDAR-derived topographic information for characterizing and differentiating landslide morphology and activity. Geomorphology *73*, 131–148. https://doi.org/10.1016/j.geomorph.2005.07.006.

76. Strahler, A.H., Muller, J., Lucht, W., Schaaf, C., Tsang, T., Gao, F., Li, X., Lewis, P., and Barnsley, M.J. (1999). MODIS BRDF/albedo product: algorithm theoretical basis document version 5.0. MODIS Doc *23*, 42–47.

77. Chakraborty, T.C., and Lee, X. (2021). Using supervised learning to develop BaRAD, a 40-year monthly bias-adjusted global gridded radiation dataset. Sci. Data *8*, 238.

78. Kaufman, Y.J., and Tanré, D. (1998). Algorithm for remote sensing of tropospheric aerosol from MODIS. NASA MODIS Algorithm Theor. Basis Doc. Goddard Space Flight Cent. *85*, 3–68.

79. Chakraborty, T., Hsu, A., Manya, D., and Sheriff, G. (2020). A spatially explicit surface urban heat island database for the United States: Characterization, uncertainties, and possible applications. ISPRS J. Photogramm. Remote Sens. *168*, 74–88. https://doi.org/10.1016/j.isprsjprs.2020.07.021.

80. Smith, R.J. (2009). Use and misuse of the reduced major axis for line-fitting. Am. J. Phys. Anthropol. *140*, 476–486.

81. Crowell, M., Edelman, S., Coulton, K., and McAfee, S. (2007). How many people live in coastal areas? J. Coast Res. *23*, iii–vi.

82. Chakraborty, T.C., Wang, J., Qian, Y., Pringle, W., Yang, Z., and Xue, P. (2023). Urban versus lake impacts on heat stress and its disparities in a shoreline city. GeoHealth *7*, e2023GH000869.

83. Breiman, L. (2001). Random forests. Mach. Learn. *45*, 5–32.

84. Rubel, F., and Kottek, M. (2010). Observed and projected climate shifts 1901-2100 depicted by world maps of the Köppen-Geiger climate classification. metz. *19*, 135–141.

85. Huang, X., Huang, J., Wen, D., and Li, J. (2021). An updated MODIS global urban extent product (MGUP) from 2001 to 2018 based on an automated mapping approach. Int. J. Appl. Earth Obs. Geoinf. *95*, 102255.

86. Gong, P., Li, X., Wang, J., Bai, Y., Chen, B., Hu, T., Liu, X., Xu, B., Yang, J., Zhang, W., and Zhou, Y. (2020). Annual maps of global artificial impervious area (GAIA) between 1985 and 2018. Remote Sens. Environ. *236*, 111510.

87. Gao, J., and O'Neill, B.C. (2020). Mapping global urban land for the 21st century with data-driven simulations and Shared Socioeconomic Pathways. Nat. Commun. *11*, 2302–2312.

88. Li, X., Zhou, Y., Asrar, G.R., and Zhu, Z. (2018). Creating a seamless 1 km resolution daily land surface temperature dataset for urban and surrounding areas in the conterminous United States. Remote Sens. Environ. *206*, 84–97.

89. Zhang, T., Zhou, Y., Zhao, K., Zhu, Z., Chen, G., Hu, J., and Wang, L. (2022). A global dataset of daily near-surface air temperature at 1-km resolution (2003–2020). Earth Syst. Sci. Data Discuss. 1–18.

Supplemental information

Urbanization exacerbates continental-

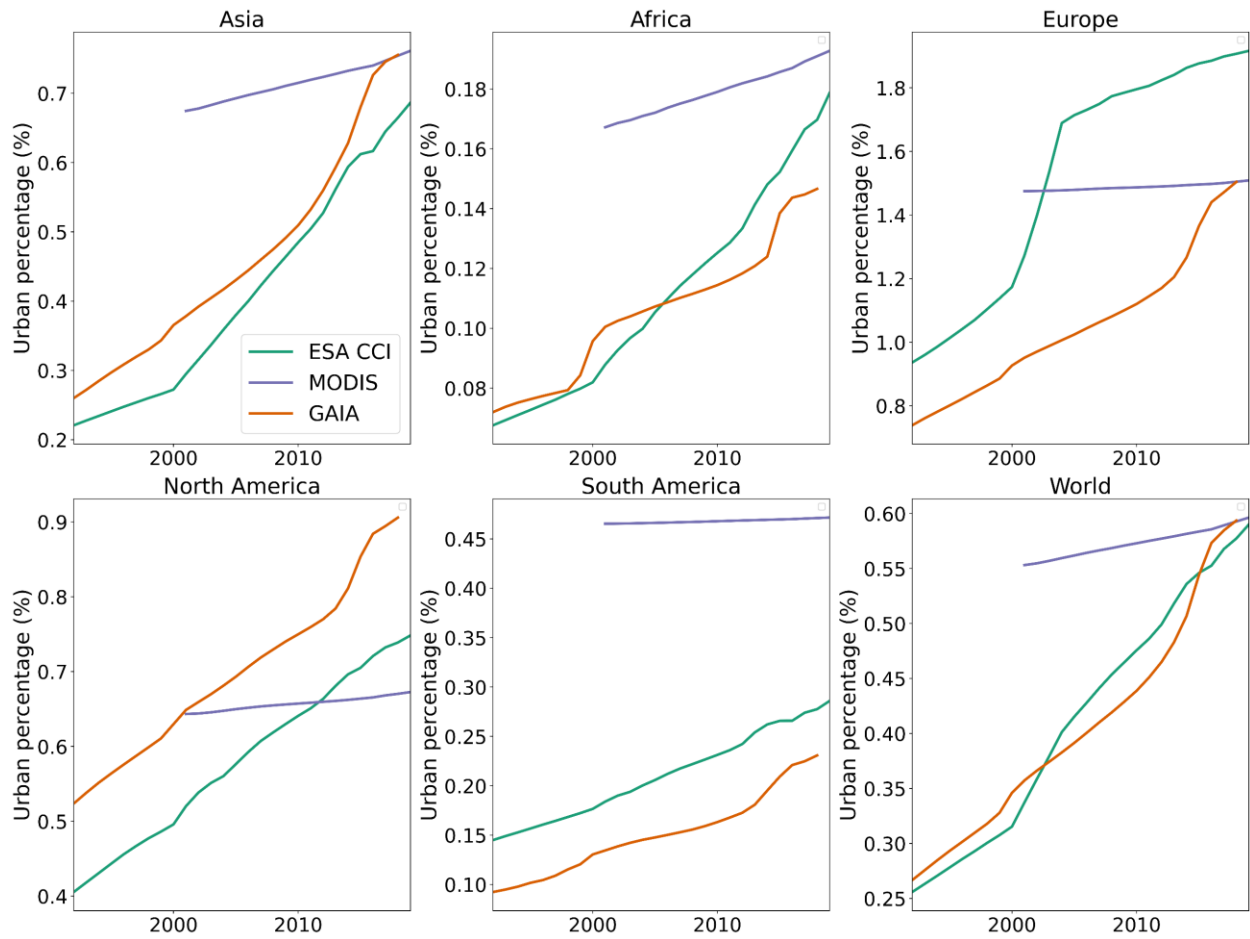# to regional-scale warming

TC Chakraborty and Yun Qian

Fig. S1. Timeseries of urban percentage from multiple datasets. Long-term trends in urban percentage for the continents and the world in the land cover datasets considered in the present study.
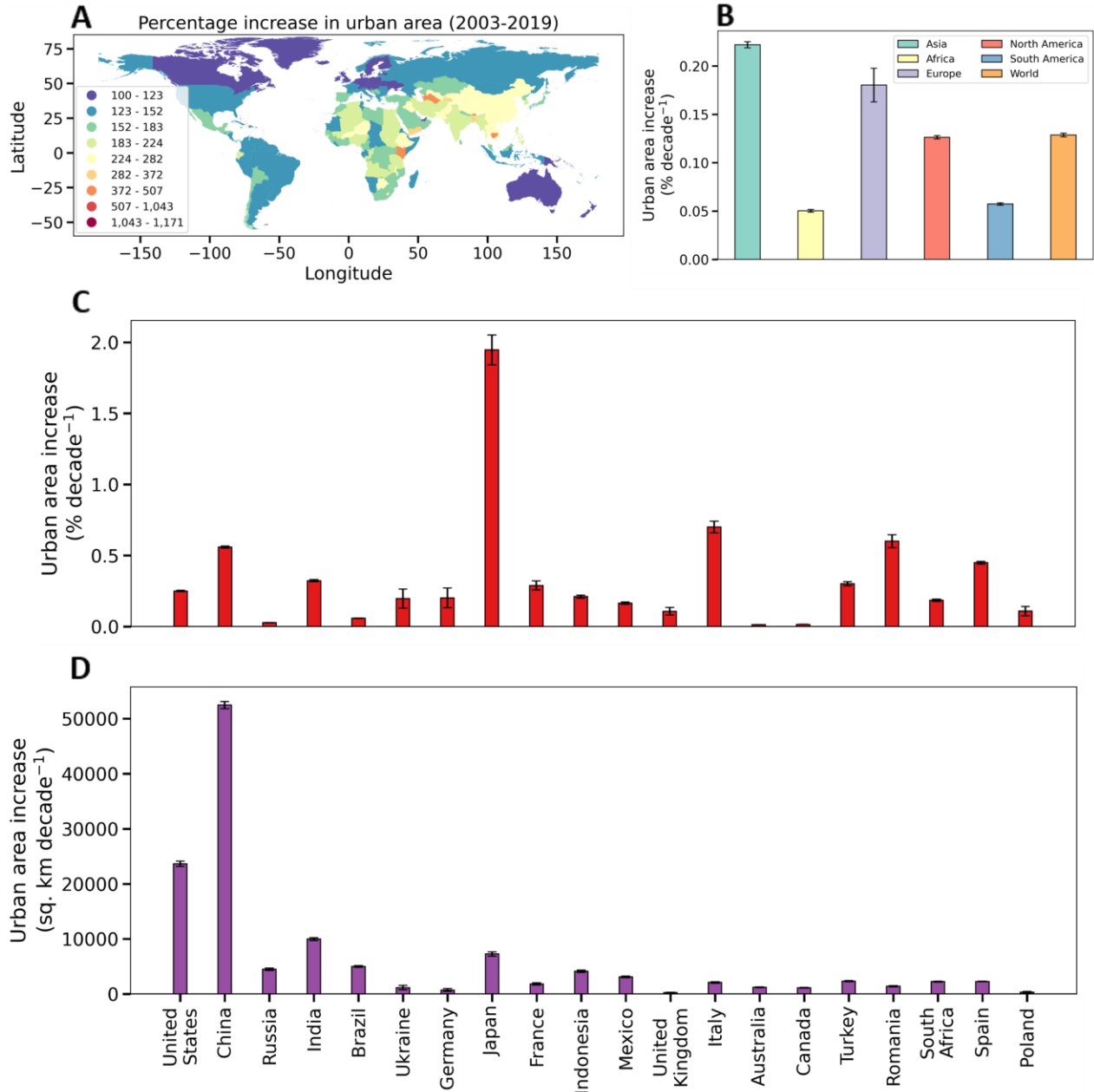
Fig. S2. Long-term changes in urban area since 2003. A shows a global map of country-wise percentage increase in urban area between 2003 and 2019. **B** and **C** show decadal rate of change in percent of urban area at the continental scale and for the twenty most urbanized countries (in 2019), respectively. **D** is similar to **E**, but for growth in urban area per decade. The error bars in **B**, **C**, and **D** give the standard errors of the slopes of the linear least-squares regressions. All changes are statistically significant ($p < 0.0001$).
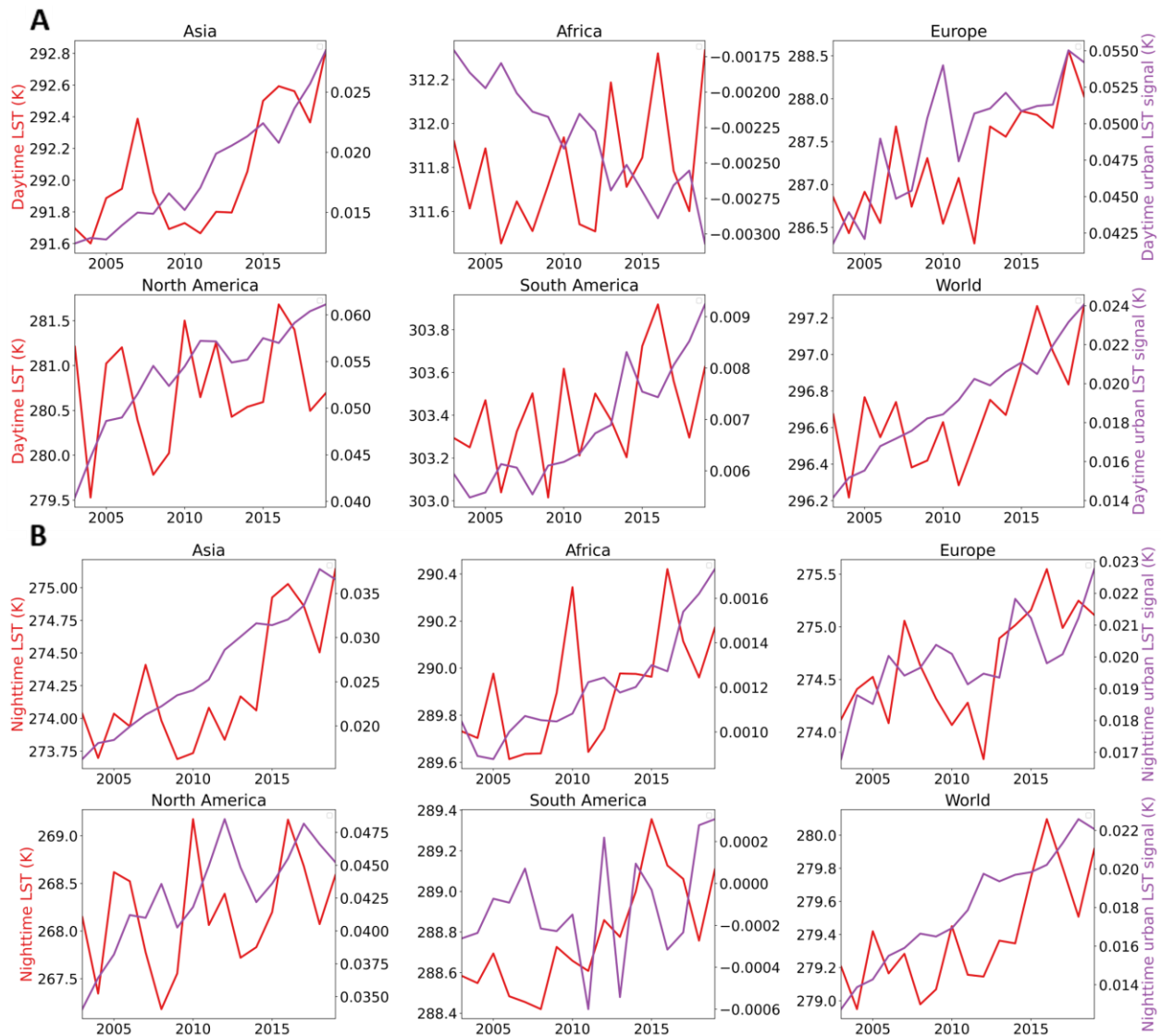
Fig. S3. Long-term trends in land surface temperature with and without the urban signal for MODIS Aqua. Long-term (2003-2019) trends in land surface temperature (LST; red) for the continents and the world, as well as the urban LST signal (purple) for each case, corresponding to the MODIS Aqua **A** daytime and **B** nighttime overpass, respectively.
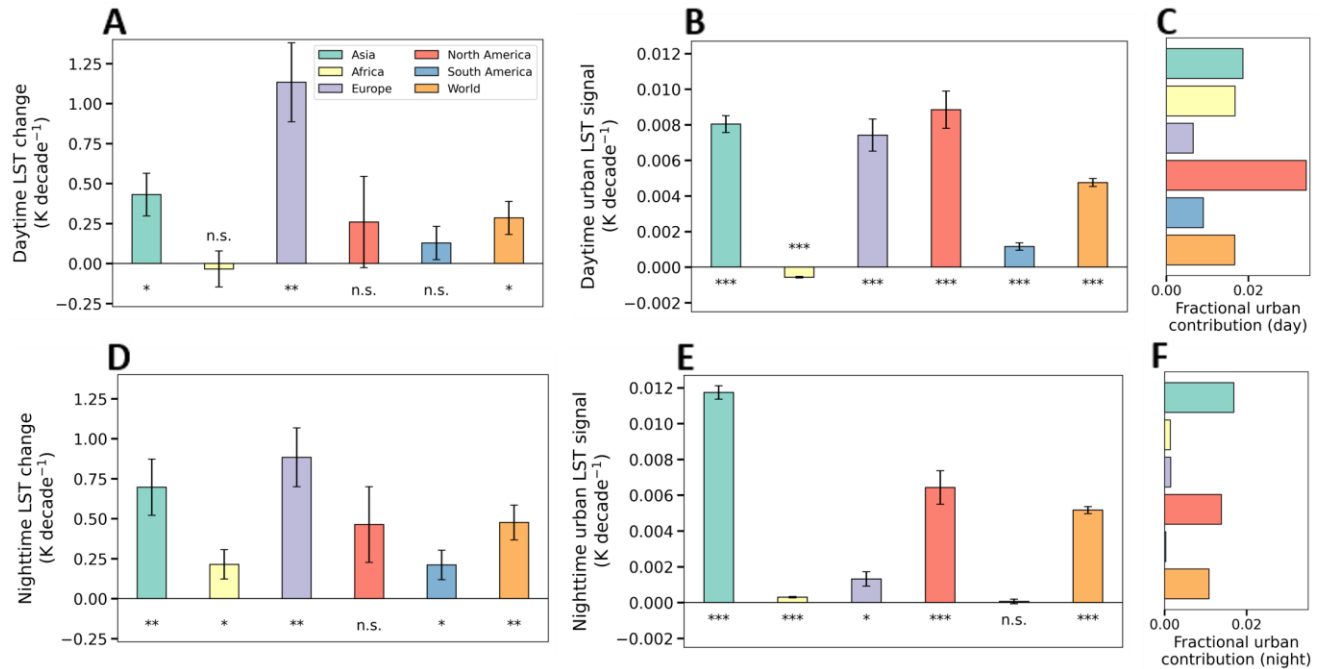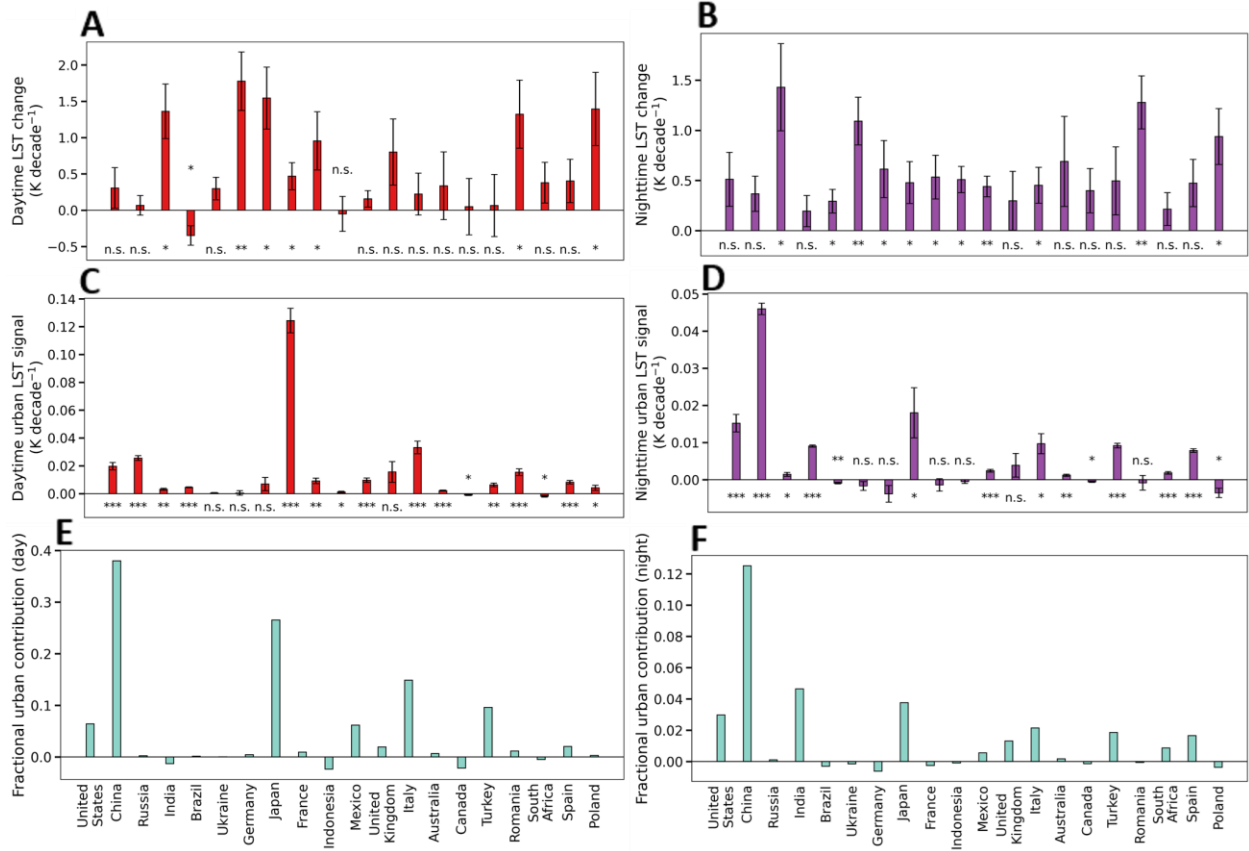
Fig. S4. Continental-scale trends in land surface temperature and urban contributions to them from MODIS Terra. A shows decadal rates of change in continental-scale and global daytime (~10:30 am local time) land surface temperature (LST) with urban pixels included based on MODIS Terra observations from 2001 to 2019. **B** isolates the contribution from only the urban pixels. **D** and **E** are similar to **A** and **B**, but for nighttime (~10:30 pm local time). **C** and **F** show the trends in the urban signal as a fraction of the overall continental-scale trends in LST. The error bars in **A**, **B**, **D**, and **E** give the standard errors of the slopes of the linear least-squares regressions and the number of * below each bar gives the level of statistical significance of the correlations (three * for p<0.0001; two * for p<0.001; one * for p<0.01; 'n.s.' for p>=0.05).
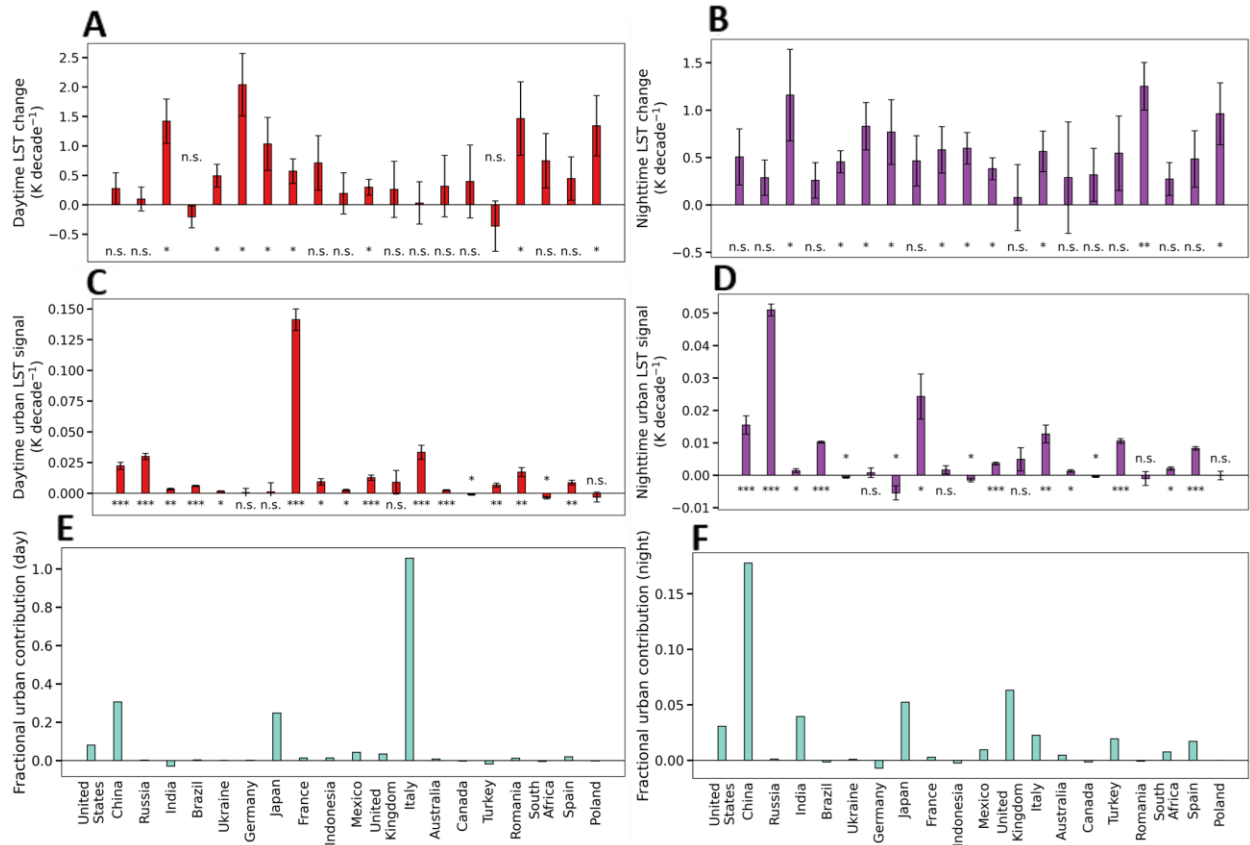
Fig. S5. Country-scale trends in land surface temperature and urban contributions to them from MODIS Aqua. A shows decadal rates of change in country-scale daytime (~1:30 pm local time) land surface temperature (LST) with urban pixels included based on satellite observations from 2003 to 2019. **C** isolates the contribution from only the urban pixels. **B** and **D** are similar to **A** and **C**, but for nighttime (~1:30 am local time). Results are shown for the twenty most urbanized countries (in 2019). The error bars give the standard errors of the slopes of the linear least-squares regressions and the number of * below each bar gives the level of statistical significance of the correlations (three * for p<0.0001; two * for p<0.001; one * for p<0.01; 'n.s.' for p>=0.05). **E** and **F** show the trends in the urban signal as a fraction of the overall country-scale trends in LST during day and night, respectively.
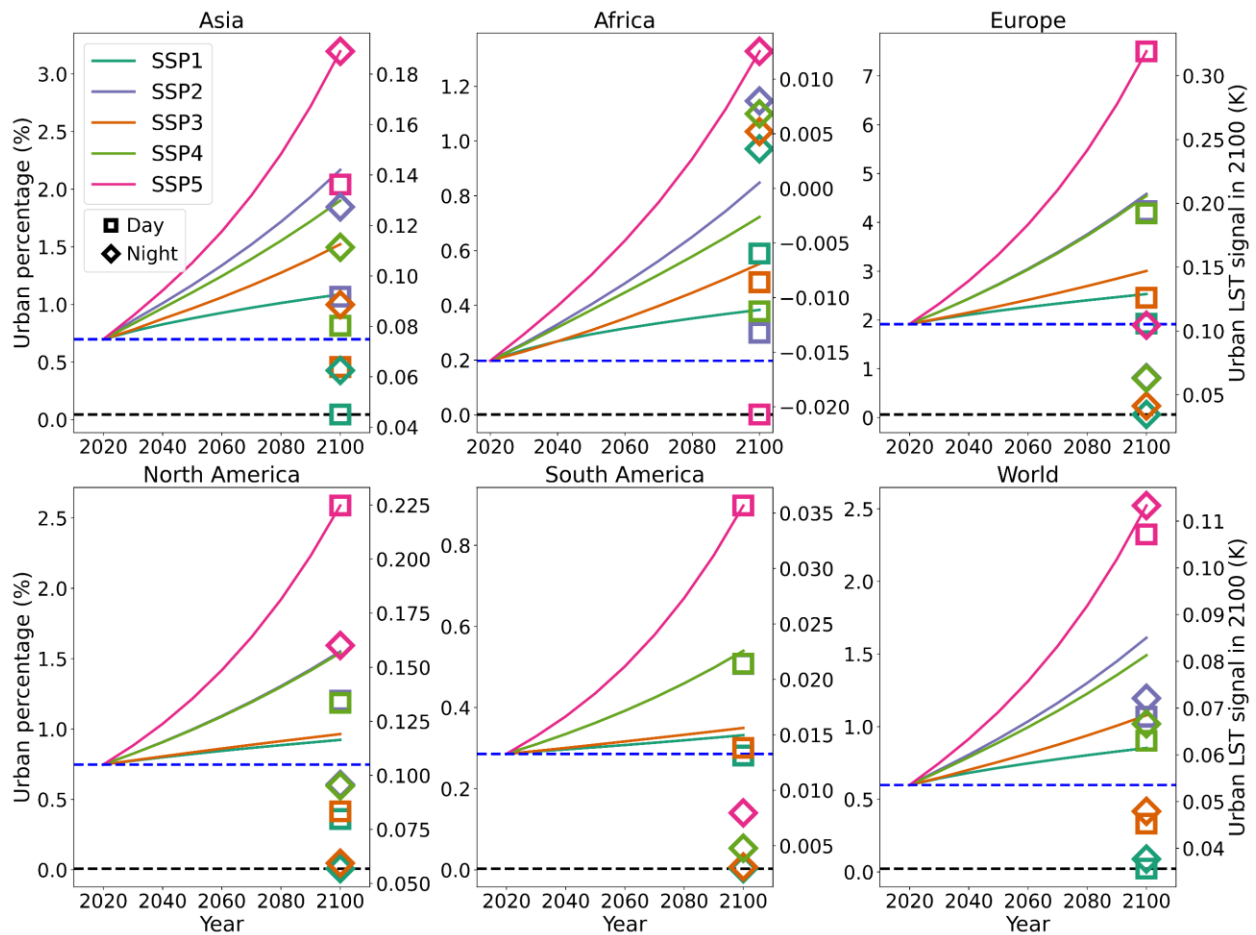
Fig. S6. Country-scale trends in land surface temperature and urban contributions to them from MODIS Terra. A shows decadal rates of change in country-scale daytime (~10:30 am local time) land surface temperature (LST) with urban pixels included based on satellite observations from 2003 to 2019. **C** isolates the contribution from only the urban pixels. **B** and **D** are similar to **A** and **C**, but for nighttime (~10:30 pm local time). Results are shown for the twenty most urbanized countries (in 2019). The error bars give the standard errors of the slopes of the linear least-squares regressions and the number of * below each bar gives the level of statistical significance of the correlations (three * for p<0.0001; two * for p<0.001; one * for p<0.01; 'n.s.' for p>=0.05). **E** and **F** show the trends in the urban signal as a fraction of the overall country-scale trends in LST during day and night, respectively.

Fig. S7. Urban temperature signal and urban percentages for shared socioeconomic pathways based on Gao and O'Neill's projections. Urban percentage for different shared socioeconomic pathways (SSPs) for the continents and the world based on 1 km global projections from Gao and O'Neill (2020). In each case, the horizontal black and blue dashed lines represent estimated urban percentage for the years 1880 and 2019, respectively. The squares and diamonds (tick labels on the right-hand y axis), colored based on SSP scenarios, represent total daytime and nighttime urban land surface temperature (LST) signals for the year 2100.
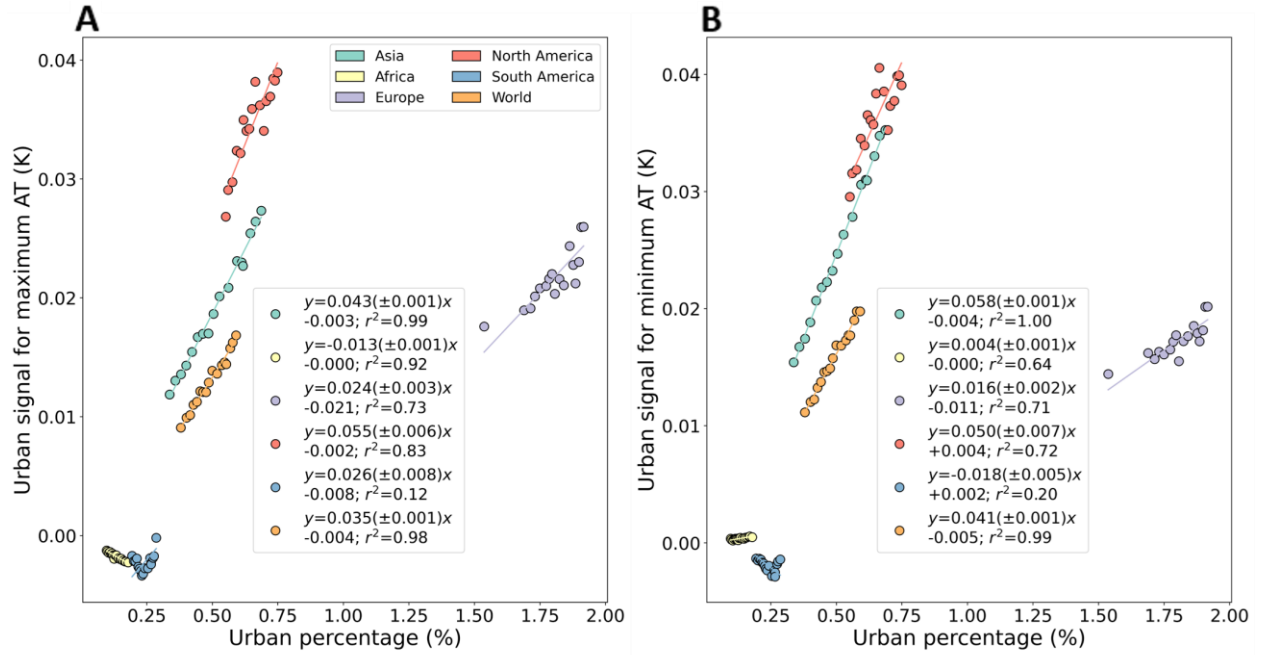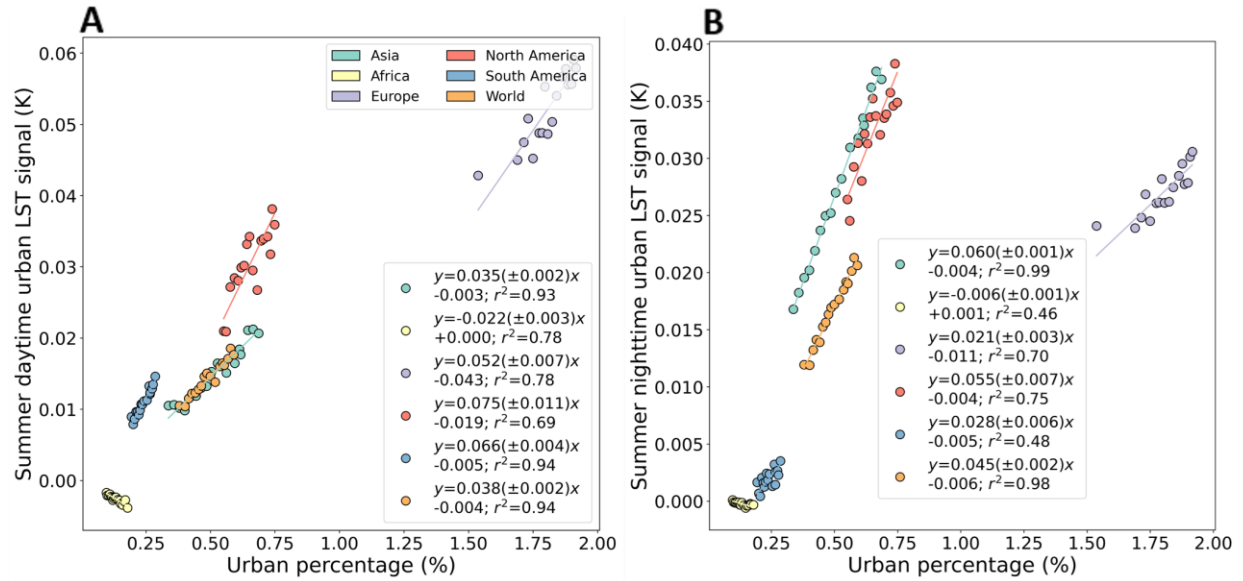
Fig. S8. Associations between the urban air temperature signal and urban percentage. A shows the associations between the yearly (2003-2019) urban signal on maximum air temperature (AT) and the corresponding urban percentage for continental and global scales. **B** is similar to **A**, but for minimum AT. The lines of best fit, including the standard errors of the slopes, and the coefficients of determination are noted for all cases.
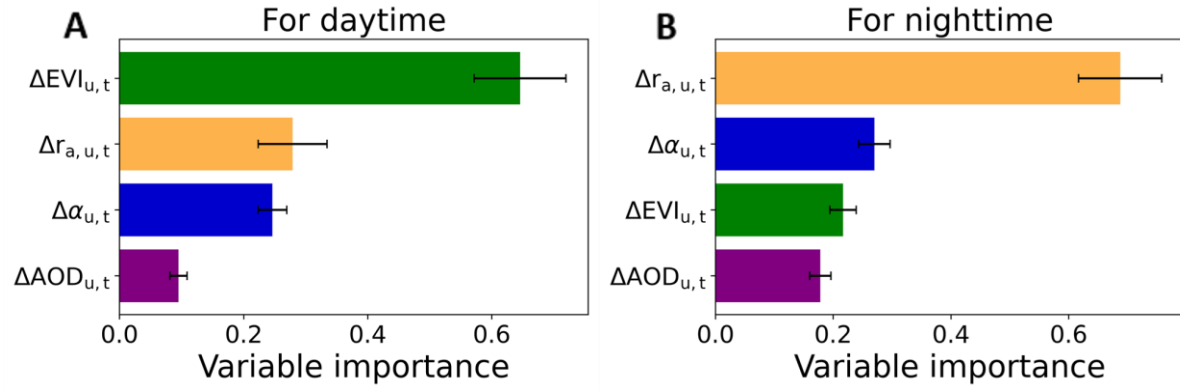
Fig. S9. Ranked variable importance scores for the urban temperature signal. Permutation importance scores for the random forest models for **A** daytime and **B** nighttime urban land surface temperature (LST) signals. The error bars show the standard deviation across the fifty model runs.
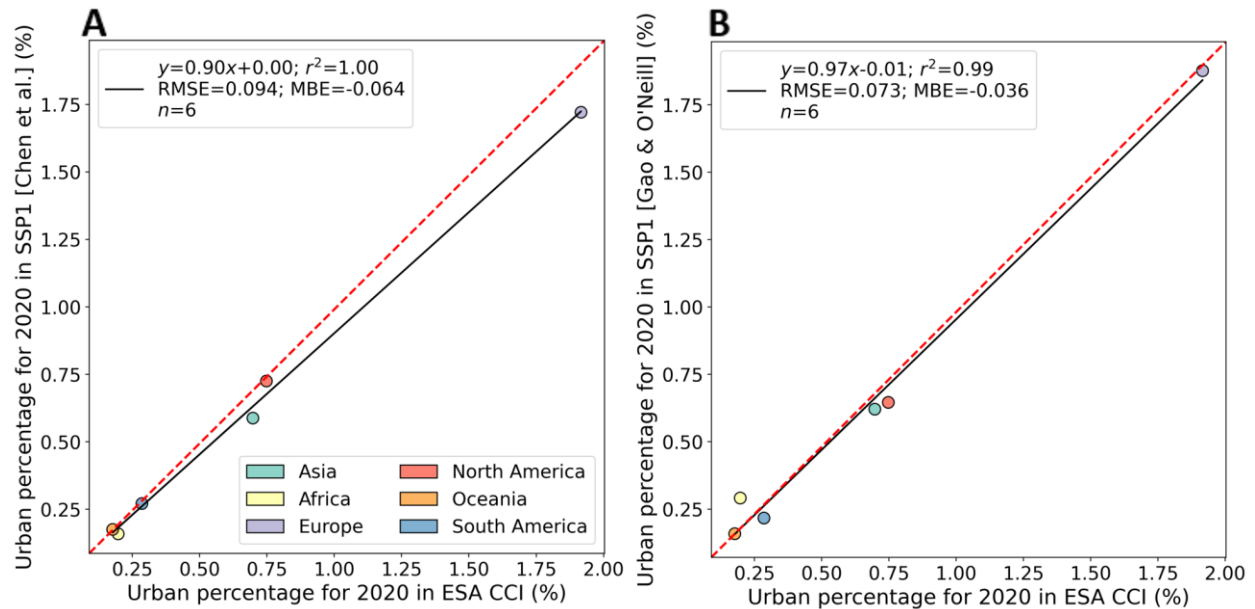
Fig. S10. Comparison between projected urban percentage and observed percentage. Comparisons between continental-scale urban percentage projection for the SSP1 scenario from **A** Chen et al. and **B** Gao & O'Neill and the observed 2020 values from the European Space Agency's Climate Change Initiative (ESA CCI) land cover dataset. Each data point corresponds to one continent (not including Seven Seas). The equation for the line of best fit, root-mean squared error (RMSE), mean bias error (MBE), and coefficient of determination (r^2) are noted.

Fig. S11. Associations between the summer temperature signal and urban percentage. A shows the associations between the yearly (2003-2019) urban signal on summer daytime (~1:30 pm local time) land surface temperature (LST) and the corresponding urban percentage for continental and global scales. **B** is similar to **A**, but for nighttime (~1:30 am local time). The lines of best fit, including the standard errors of the slopes, and the coefficients of determination are noted for all cases.
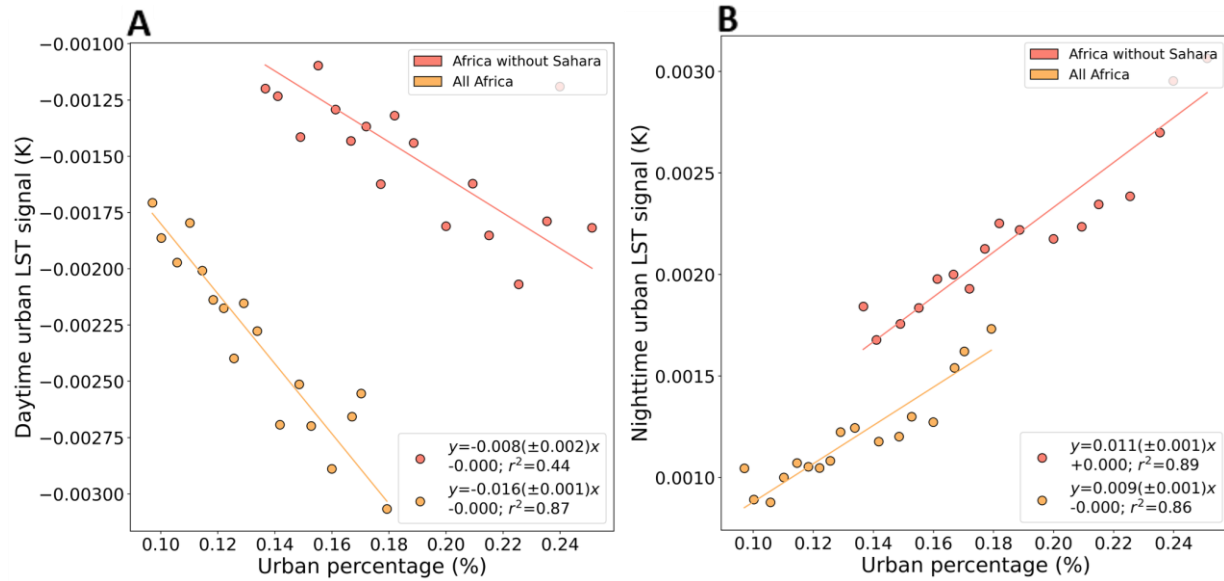
Fig. S12. Impact of selection of regions on continental scale signal over Africa. A shows the associations between the yearly (2003-2019) urban signal on summer daytime (~1:30 pm local time) land surface temperature (LST) and the corresponding urban percentage for continental and global scales. **B** is similar to **A**, but for nighttime (~1:30 am local time). The lines of best fit, including the standard errors of the slopes, and the coefficients of determination are noted for all cases.
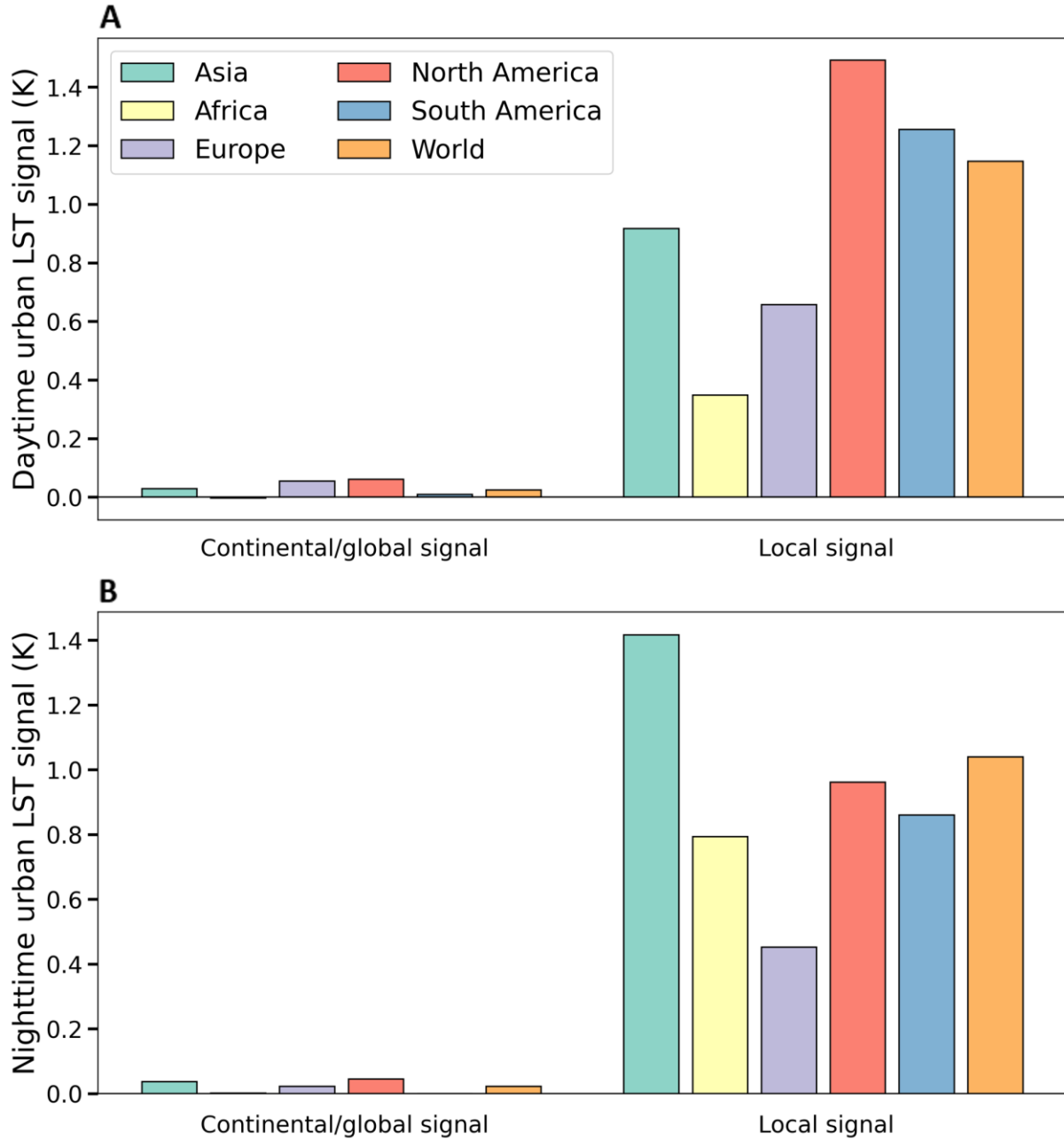
Fig. S13. Comparisons between local and global urban land surface temperature signals. A shows urban signal on daytime (~1:30 pm local time) land surface temperature (LST) for the year 2019 at the continental/global scale, using the approach of the present study, and at the local scale, which is equivalent to surface urban heat island estimates. **B** is similar to **A**, but for nighttime (~1:30 am local time).
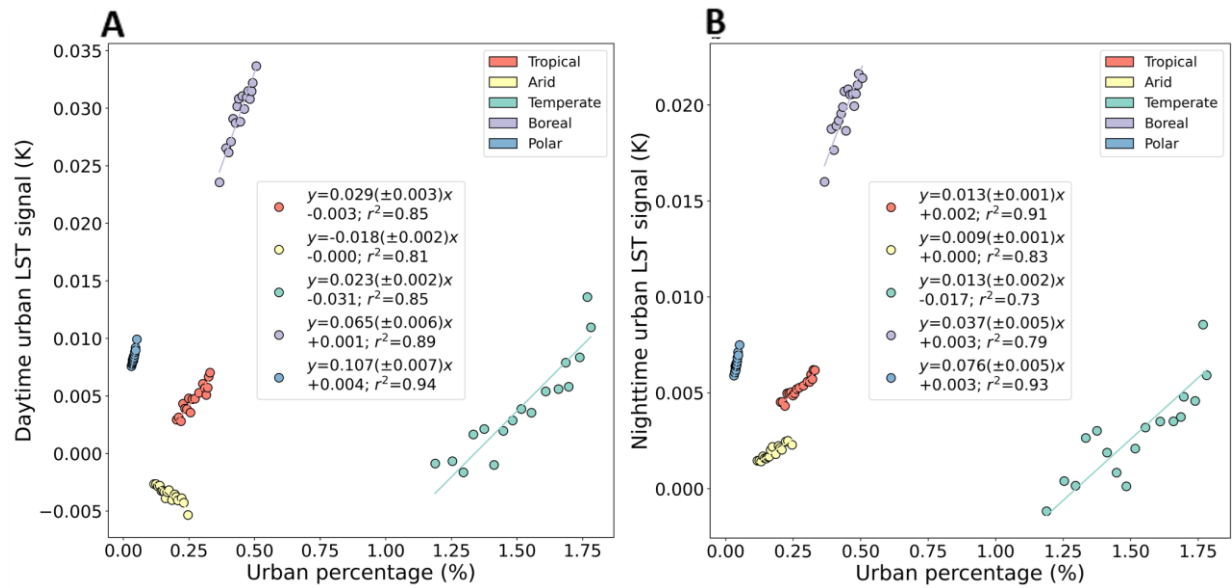
Fig. S14. Associations between urban temperature signal and urban percentage by climate zone. A shows associations between the yearly (2003-2019) urban signal on daytime (~1:30 pm local time) land surface temperature (LST) and corresponding urban percentage for all Köppen-Geiger climate zones. **B** is similar to **A**, but for nighttime (~1:30 am local time). The lines of best fit, including standard errors of the slopes, and coefficients of determination are noted for all cases.
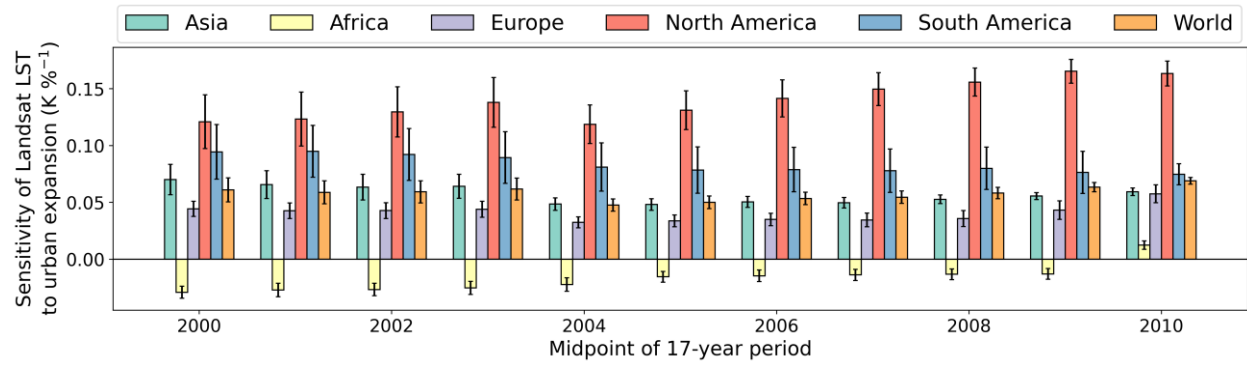
Fig. S15. Choice of subperiod of analysis and sensitivity of urban temperature signal to urban percentage. Sensitivities (slopes; standard errors of slopes given by the error bars) of the urban land surface temperature (LST) signal to urbanization for all possible 17-year consecutive time period within 1992 and 2019 based on Landsat LST for all continents and the world.
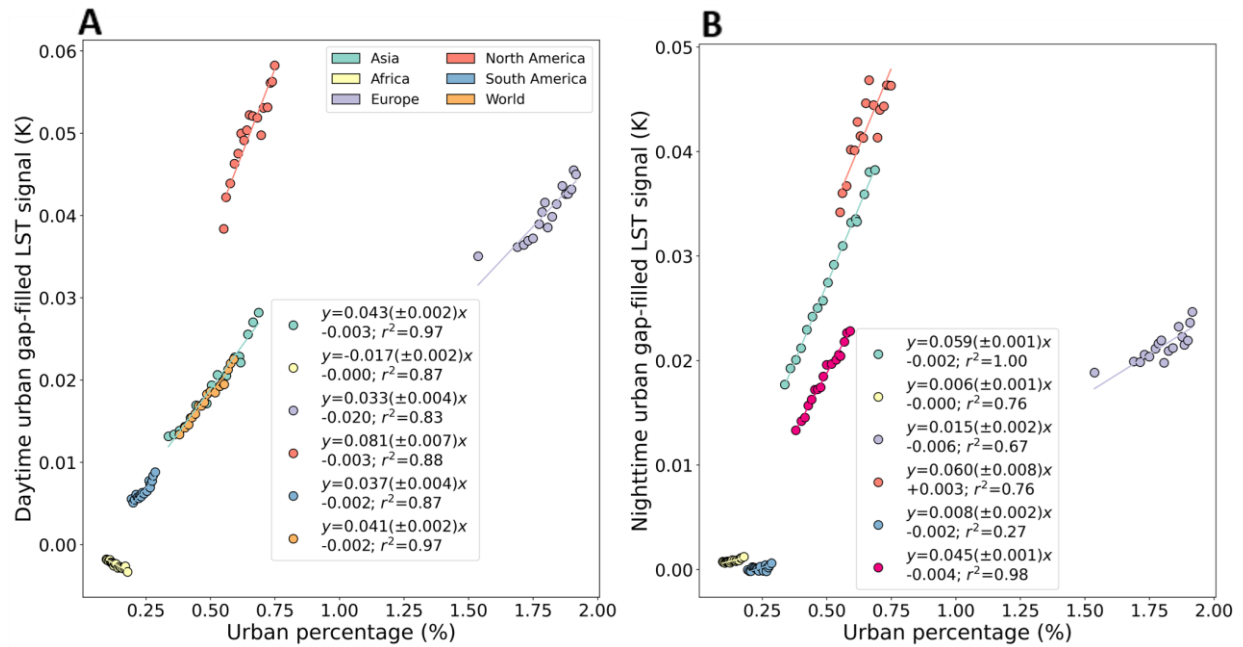
Fig. S16. Associations between the urban temperature signal and urban percentage using gap-filled LST. A shows the associations between the yearly (2003-2019) urban signal on midday gap-filled land surface temperature (LST) and the corresponding urban percentage for continental and global scales. **B** is similar to **A**, but for midnight. The lines of best fit, including the standard errors of the slopes, and the coefficients of determination are noted for all cases.